

Dynamic Interaction Analysis of Maglev-Guideway System Based on a 3D Full Vehicle Model

Dong-Ju Min*, Myung-Rag Jung[†] and Moon-Young Kim[‡]

*Department of Civil and Environmental Engineering
Sungkyunkwan University, 440-746 Suwon
Jangan-gu, Cheoncheon-Dong, South Korea*

**marshow@nate.com*

†psjehun@naver.com

‡kmye@skku.edu

Jong-Won Kwark

*Structural Engineering Research Division
SOC Research Institute, 411-712 Goyang
Ilсанseo-gu, Daehwa-Dong, South Korea
origilon@kict.re.kr*

Received 26 May 2015

Accepted 31 December 2015

Published 14 March 2016

The purpose of this paper is to develop a detailed 3D maglev vehicle and guideway model and investigate the dynamic response characteristics of the coupled system. For this, the maglev vehicle is modeled as one cabin and four bogies having eight electromagnetics, four sensors, and four secondary suspensions based on the Urban Transit Maglev (UTM) system in Korea. The 3D dynamic equilibrium equations of the cabin and bogies are derived by considering the actively controlled electromagnetic forces. Also, the equations of motion for the guideway are derived using the modal superposition method for vertical, lateral, and torsional modes. The resulting coupled equations of motion are then solved using a predictor-corrector iterative algorithm. Finally, through the numerical simulation of the developed system, the responses using the 3D maglev vehicle model are compared with those obtained by the corresponding 2D model. The effects of surface irregularity on the dynamic interaction behaviors are then evaluated for increasing vehicle speeds. Particularly, the 3D resonance conditions of the guideway girder and the maglev vehicle are presented considering the resonance conditions due to equidistant moving loads. In addition, some resonance phenomena are rigorously explored, including the lateral resonance by a series of vehicles running on a girder.

Keywords: Maglev vehicle; guideway structure; dynamic interaction; resonance condition; surface irregularity; EMS; mode superposition.

*Corresponding author.

1. Introduction

The research and development of the maglev vehicle system has been actively carried out in many countries since the 1970s. The maglev vehicle is operated by using magnetic levitation forces, and there are two types of magnetic levitation systems: the electromagnetic system (EMS) and the electrodynamic system (EDS). Based on the principle of attraction in magnetism, the EMS vehicles installed with the conventional electromagnets are attracted upward toward the ferromagnetic rails above the magnets. In contrast, based on the principle of repulsion in magnetism, the EDS vehicles installed with magnets, when moving over the conductor rail, induce the conductor eddy currents and produce a magnetic field that repels the magnets on the vehicles.¹

On the other hand, the maglev vehicle provides excellent qualities such as comfortable ride, anti-noise feature, reduced risk of derailment, and reduced cost for guideway maintenance in comparison with the conventional wheel-rail system.² Due to its superiority, the test line for maglev was competitively constructed in Germany and Japan. As a result, the Japanese MLX01 maglev vehicle and the Shanghai Maglev Train (SMT) were developed in 2003 and 2001, respectively. The urban transit maglev (UTM) system is currently being developed in Korea to provide effective transportation in metropolitan areas and its commercial service is expected to be launched in 2015. Figure 1 shows a new version of the maglev vehicle running on a short test line which underwent a trial performance in 2010.

The maglev vehicle is regarded as a transportation system for the near future. Between the 1970s and 1980s, most of the studies were conducted in Germany³⁻⁵ and Japan.^{6,7} Since the 1990s, numerous studies on the maglev system have been performed and have led to remarkable progress in many countries.

In China, Zheng *et al.*⁸ performed a numerical simulation of a coupled 5-degree-of-freedom (DOF) maglev vehicle and guideway system with a controllable feedback magnetic force. Zhao and Zhai⁹ investigated the ride quality of a two-dimensional



Fig. 1. UTM vehicle on test track (Korea).

(2D) model of the German Transrapid maglev vehicle with an equivalent passive suspension running on a simple beam. Wang *et al.*¹⁰ performed a numerical dynamic simulation of the maglev vehicle and guideway system. Yang *et al.*¹¹ investigated the robust control of a class of uncertain systems via a disturbance-observer-based control approach, the control method of which was applied to a nonlinear maglev system. Shi *et al.*¹² studied the dynamic response of the single-span guideway induced by a moving maglev train, while analyzing the resonant conditions of a single-span guideway for the vertical direction.

In the USA, Cai *et al.*¹³ performed a parametric study on short span bridges crossed by a 2-DOF maglev vehicle with passive spring and dashpot suspension. Fang *et al.*¹⁴ studied the dynamic modeling and control of the Magplane vehicle. Kaloust *et al.*¹⁵ presented a nonlinear robust control design for the levitation and propulsion of a magnetic levitation that guarantees global stability and robustness for a nonlinear 2-DOF maglev system.

Also, Huang *et al.*¹⁶ in Taiwan proposed a nonlinear adaptive back-stepping controller to stabilize the system under model uncertainty and achieve the desired servo performance in a 5-DOF system. Yau^{17–20} performed a numerical simulation for vibration and control analysis of maglev vehicles under diverse situations, such as wind and horizontal ground motion. Also, Yau²⁰ investigated the resonance phenomena regarding the vertical response of the guideway in the maglev system.

In Iran, Yaghoubi and Rezvani²¹ studied the development of the maglev guideway loading model. Shibo *et al.*²² in the Netherlands presented coupled analysis results for the maglev vehicle and guideway system using Simulink to solve the coupled problem. In Korea, Han *et al.*²³ performed a finite element based numerical simulation of the Korean UTM vehicle and guideway structures by using a large number of elements. Also, Jin *et al.*²⁴ proposed an optimized maglev guideway system that fulfills the requirements of the Center for Urban Maglev Program. Kwon *et al.*²⁵ performed a numerical simulation for a 5-DOF maglev vehicle with equivalent passive suspension running on a suspension bridge under gusty winds in order to test the applicability of such a flexible bridge for the guideway structure. Lee *et al.*²⁶ developed a numerical model for the dynamic interaction analysis of an actively controlled 5-DOF maglev vehicle and flexible guideway structure.

Generally, most studies have been carried out for a 2D maglev model, and few studies have employed an actively controlled 3D model, except for the simplified 4-DOF maglev model by Yau.²⁰ It seems that the simplified model cannot accurately reflect the dynamic characteristics of the realistic maglev model.

In this paper, a detailed 3D vehicle model based on the UTM vehicle is newly developed for an actively controlled maglev-guideway system, with the dynamic interaction effect of the guideway and maglev vehicle investigated using the developed model. The dynamic equations of a 25-DOF maglev vehicle model consisting of one cabin and four bogies are derived by expanding the works conducted thus far on the 2D model.^{26,27} The equations of motion for the guideway are obtained using the

modal superposition method, and the active control algorithm adopted in the UTM controller is used to control the magnetic force. The resulting coupled equations of the vehicle are solved using an iterative scheme with the Newmark- β method. Finally, numerical analyses are conducted to demonstrate the validity and accuracy of the present interaction model. Particularly, the 3D resonance conditions of the guideway girder or the maglev vehicle are presented with consideration of the resonance conditions due to equidistant moving loads. In addition, a number of resonance phenomena are rigorously explored, including the lateral resonance by a series of vehicles running on a girder.

2. Maglev Vehicle Model

A detailed 3D maglev model is introduced and the equations of motion for the maglev vehicle are derived considering the electromagnetic vertical and lateral forces of the EMS in this section.

2.1. 3D maglev vehicle model

Figure 2 shows a detailed 3D maglev vehicle model based on the UTM vehicle. The vehicle model in Fig. 2 is shown as an upturned configuration to represent the attraction force between the electromagnet attached to the bogie and the reaction plate of the guideway. The maglev vehicle consists of one cabin and four bogies linked by secondary suspension springs, in which the cabin and the bogies are assumed to be rigid bodies having 5-DOF such as lateral and vertical displacements (y, z) and rolling, pitching and yawing rotations ($\theta_x, \theta_y, \theta_z$), except for the running direction x . Secondary suspensions involving springs and dashpots in the vertical and lateral directions are located between the cabin and bogies as shown in Fig. 2. Also, each bogie has eight electromagnets generating levitation forces and four sensors measuring both the air gap and acceleration (Fig. 2(c)). Thus, one vehicle model has a total of 25-DOF, and the geometric and the material properties of the UTM model are listed in Tables 1 and 2, respectively, in which the subscripts j , k , s , and i represent the order of four bogies, eight electromagnets, four sensors, and four secondary suspensions per bogie, respectively.

2.2. Dynamic equilibrium equations of cabin

Figure 3 shows the free body diagram of a cabin separated from the four bogies, in which the cabin is subjected to vertical forces only, such as the vertical inertia force, vertical spring and damping forces of the secondary suspensions, and the self-weight. First, the equilibrium equation of the cabin under its self-weight at the static state is

$$\sum_{j=1}^{N_{\text{bogi}}} \sum_{i=1}^{N_{\text{spring}}} F_{sjizo} = m_c g, \quad (1)$$

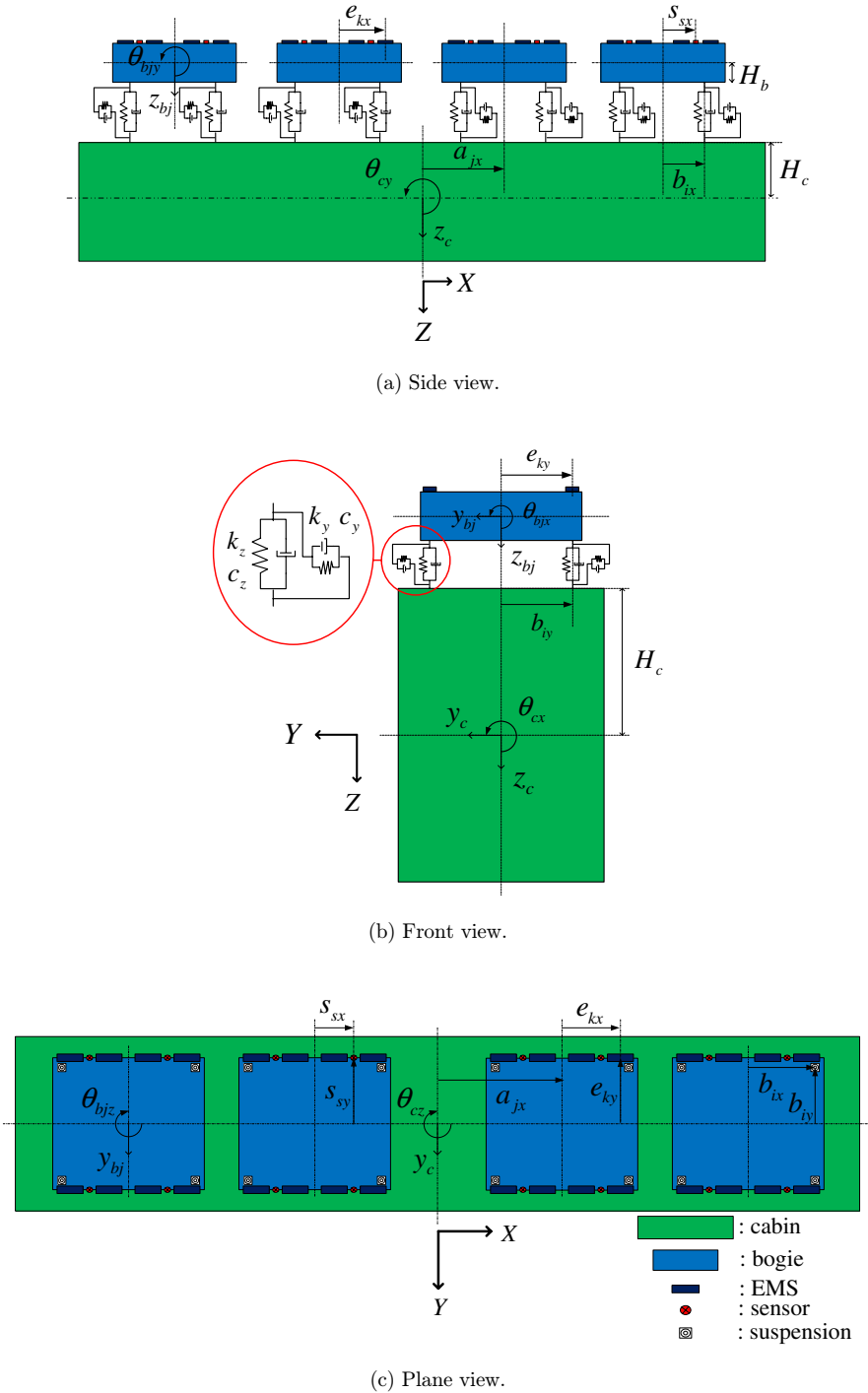


Fig. 2. 3D maglev vehicle model.

Table 1. Geometric properties of the UTM vehicle model.

Index	Number of elements	Value (m)
a_{jx}	$j = 1, 2, 3, 4$	4.05, 1.35, -1.35, -4.05
e_{kx}	$k = 1, 2, \dots, 8$	1.005, 0.415, 1.005, 0.415, -0.415, -1.005, -0.415, -1.005
e_{ky}		0.5, 0.5, -0.5, -0.5, 0.5, 0.5, -0.5, -0.5
s_{sx}	$s = 1, 2, 3, 4$	0.71, 0.71, -0.71, -0.71
s_{sy}		0.925, -0.925, 0.925, -0.925
b_{ix}	$i = 1, 2, 3, 4$	1.08, 1.08, -1.08, -1.08
b_{iy}		0.925, -0.925, 0.925, -0.925
H_c, H_b	—	1.36, 0.071

Table 2. Material properties of the UTM vehicle model.

Index	Value
Mass of cabin (m_c)	19000 kg
Mass moments of inertia of cabin (I_{cx}, I_{cy}, I_{cz})	22364, 141900, 132800 kg · m ²
Mass of bogie (m_b)	1015 kg
Mass moments of inertia of bogie (I_{bx}, I_{by}, I_{bz})	67.1, 557.8, 542.8 kg · m ²
Spring coefficients of secondary suspension (k_y, k_z)	$1.5 \times 10^4, 2 \times 10^4$ N/m
Damping coefficients of secondary suspension (c_y, c_z)	$1.6 \times 10^3, 1.3 \times 10^3$ N · s/m
Properties of electromagnet (μ_o, N_m, A_m, R_m)	$4\pi \times 10^{-7}, 400, 0.036$ m ² , 0.6 Ω

where F_{sjizo} = the static spring forces of the secondary suspensions, and m_c = mass of the cabin. The dynamic equilibrium equation of the cabin in the vertical direction can then be obtained from Fig. 3 as follows:

$$m_c \ddot{z}_c = - \sum_{j=1}^{N_{bogi}} \sum_{i=1}^{N_{spring}} (k_z z_{cbji} + c_z \dot{z}_{cbji} + F_{sjizo}) + m_c g, \quad (2)$$

where z_{cbji} and \dot{z}_{cbji} = the relative vertical displacement and velocity between the cabin and the j th bogie at the i th secondary suspension, which can be expressed as

$$z_{cbji} = \{z_c - (a_{jx} + b_{ix})\theta_{cy} + b_{iy}\theta_{cx}\} - \{z_{bj} - b_{ix}\theta_{by} + b_{iy}\theta_{bx}\}, \quad (3)$$

$$\dot{z}_{cbji} = \{\dot{z}_c - (a_{jx} + b_{ix})\dot{\theta}_{cy} + b_{iy}\dot{\theta}_{cx}\} - \{\dot{z}_{bj} - b_{ix}\dot{\theta}_{by} + b_{iy}\dot{\theta}_{bx}\}. \quad (4)$$

Then, subtracting Eq. (1) from Eq. (2) leads to

$$m_c \ddot{z}_c = - \sum_{j=1}^{N_{bogi}} \sum_{i=1}^{N_{spring}} (k_z z_{cbji} + c_z \dot{z}_{cbji}). \quad (5)$$

Finally, the dynamic equilibrium equations of the cabin for the lateral, rolling, pitching and yawing motions are derived by the same procedure as follows:

$$m_c \ddot{y}_c = - \sum_{j=1}^{N_{bogi}} \sum_{i=1}^{N_{spring}} (k_y y_{cbji} + c_y \dot{y}_{cbji}), \quad (6)$$

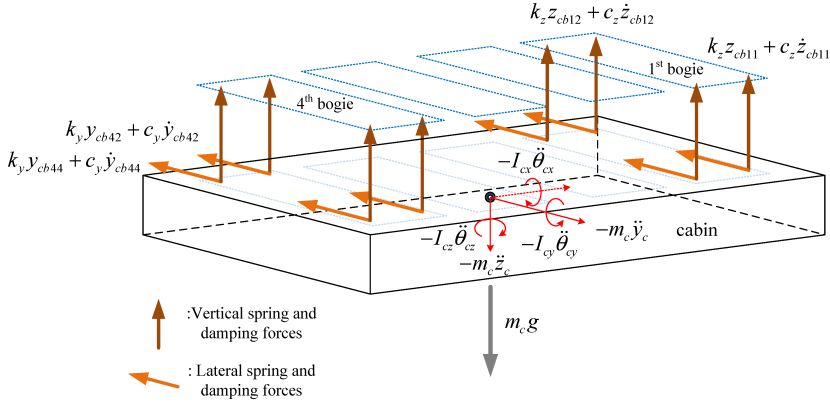


Fig. 3. Free body diagram of a cabin.

$$I_{cx} \ddot{\theta}_{cx} = - \sum_{j=1}^{N_{\text{bogi}}} \sum_{i=1}^{N_{\text{spring}}} \{b_{iy} (k_z z_{cbji} + c_z \dot{z}_{cbji} + H_c (k_y y_{cbji} + c_y \dot{y}_{cbji}))\}, \quad (7)$$

$$I_{cy} \ddot{\theta}_{cy} = \sum_{j=1}^{N_{\text{bogi}}} \sum_{i=1}^{N_{\text{spring}}} \{(a_{jx} + b_{ix}) (k_z z_{cbji} + c_z \dot{z}_{cbji})\}, \quad (8)$$

$$I_{cz} \ddot{\theta}_{cz} = - \sum_{j=1}^{N_{\text{bogi}}} \sum_{i=1}^{N_{\text{spring}}} \{(a_{jx} + b_{ix}) (k_y y_{cbji} + c_y \dot{y}_{cbji})\}, \quad (9)$$

where y_{cbji} and \dot{y}_{cbji} are the relative lateral displacement and velocity, respectively, which can be expressed as

$$y_{cbji} = \{y_c + H_c \theta_{cx} + (a_{jx} + b_{ix}) \theta_{cz}\} - \{y_{bj} - H_b \theta_{bjx} + b_{ix} \theta_{bjz}\}, \quad (10)$$

$$\dot{y}_{cbji} = \{\dot{y}_c + H_c \dot{\theta}_{cx} + (a_{jx} + b_{ix}) \dot{\theta}_{cz}\} - \{\dot{y}_{bj} - H_b \dot{\theta}_{bjx} + b_{ix} \dot{\theta}_{bjz}\}. \quad (11)$$

2.3. Dynamic equilibrium equations of bogies

Before deriving the equations of motion for the bogies, the equilibrium equation of the entire vehicle under self-weight at the static state needs to be written,

$$\sum_{j=1}^{N_{\text{bogi}}} \sum_{k=1}^{N_{\text{ems}}} F_{ejkzo} = m_c g + \sum_{j=1}^{N_{\text{bogi}}} m_{bj} g, \quad (12)$$

where the initial static equilibrium force F_{ejkzo} is equal to the total weight of the vehicle divided by the number of electromagnets. Using F_{ejkz} and F_{ejky} to denote the levitation and guidance forces, respectively, generated from the k th electromagnet of the j th bogie, the total levitation force can be separated into the initial static force F_{ejkzo} and fluctuating force ΔF_{ejkz} .

Generally, the bogies of the maglev vehicle are subjected to the electromagnetic forces of the EMS as well as the spring and damping forces of the secondary suspensions. Figure 4 depicts a free body diagram of one bogie subjected to the forces related to the rolling motion, namely the rolling inertia moment, the spring and damping forces of the secondary suspensions, and the levitation and guidance forces generated from the electromagnet. Consequently, the equation of rolling motion for each bogie can be obtained from Fig. 4 as follows:

$$I_{bjx} \ddot{\theta}_{bjx} = \sum_{i=1}^{N_{\text{spring}}} \{b_{iy}(k_z z_{cbji} + c_z \dot{z}_{cbji}) - H_b(k_y y_{cbji} + c_y \dot{y}_{cbji})\} + \sum_{k=1}^{N_{\text{ems}}} (-H_b \Delta F_{ejky} - e_{ky} \Delta F_{ejkz}). \quad (13)$$

Furthermore, the remaining equations of motion for each bogie can be constructed by the same procedure as follows:

$$m_{bj} \ddot{z}_{bj} = \sum_{i=1}^{N_{\text{spring}}} (k_z z_{cbji} + c_z \dot{z}_{cbji}) - \sum_{k=1}^{N_{\text{ems}}} \Delta F_{ejkz}, \quad (14)$$

$$m_{bj} \ddot{y}_{bj} = \sum_{i=1}^{N_{\text{spring}}} (k_y y_{cbji} + c_y \dot{y}_{cbji}) - \sum_{k=1}^{N_{\text{ems}}} \Delta F_{ejky}, \quad (15)$$

$$I_{bjy} \ddot{\theta}_{bjy} = - \sum_{i=1}^{N_{\text{spring}}} b_{ix}(k_z z_{cbji} + c_z \dot{z}_{cbji}) + \sum_{k=1}^{N_{\text{ems}}} e_{kx} \Delta F_{ejkz}, \quad (16)$$

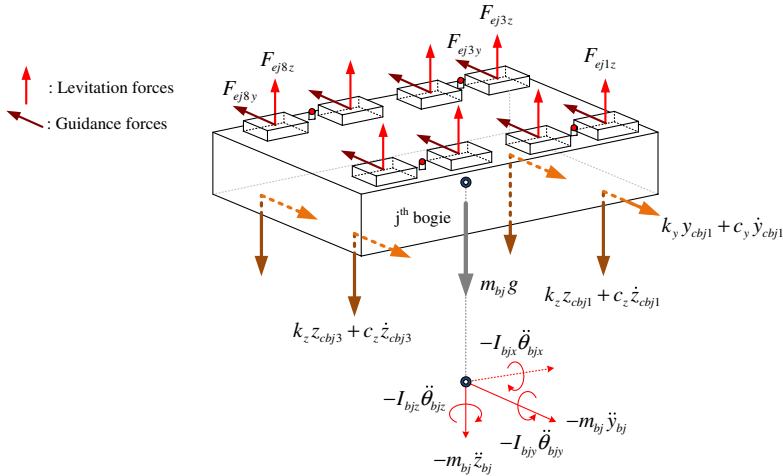


Fig. 4. Free body diagram of a bogie.

$$I_{bjz}\ddot{\theta}_{bjz} = \sum_{i=1}^{N_{\text{spring}}} b_{ix}(k_y y_{cbji} + c_y \dot{y}_{cbji}) - \sum_{k=1}^{N_{\text{ems}}} e_{kx} \Delta F_{ejky}. \quad (17)$$

2.4. Electromagnetic force

Clearly, the sum of the magnetic forces generated by electromagnets should equal the total weight of the maglev vehicle and passengers. The electromagnetic force can be calculated from the attractive force between the electromagnets attached at the bogies and the ferromagnetic objects on the guideway. Ignoring the disturbance force, the total levitation force acting on a track is evaluated with respect to the current and air-gap as²⁸:

$$F_{ejkz} = \frac{\mu_o N_m^2 A_m}{4} \left[\frac{i_o + \Delta i_{jk}}{z_o + \Delta z_{gbjk}} \right]^2, \quad (18)$$

$$v_o + \Delta v_{js} = R_m \{i_o + \Delta i_{js}\} + \frac{\mu_o N_m^2 A_m}{2} \frac{d}{dt} \left[\frac{i_o + \Delta i_{js}}{z_o + \Delta z_{gbjs}} \right], \quad (19)$$

where v_o, i_o, z_o = the initial voltage, current, and air gap at static equilibrium state, respectively. In addition, μ_o = the magnetic permeability of vacuum; N_m = the number of turns of the magnetic coil; A_m = the effective area of the magnetic pole; and R_m = the reluctance of the magnet circuit. Here, the subscripts o and Δ denote the value at the static levitated state and its increment, respectively. Also, Δz_{gbjk} and Δz_{gbjs} indicate the vertical air-gaps between the guideway and the j th bogie, and the s th sensor at the k th electromagnet, respectively, expressed as

$$\Delta z_{gbjk} = z_{bj} - e_{kx} \theta_{bjy} + e_{ky} \theta_{bjx} - z_{rjk} - z_{gjk}, \quad (20)$$

$$\Delta z_{gbjs} = z_{bj} - s_{sx} \theta_{bjy} + s_{sy} \theta_{bjx} - z_{rjs} - z_{gjs}. \quad (21)$$

For a linear system, Eqs. (18) and (19) can be simplified as follows:

$$F_{ejkz} = F_{ejkzo} + \Delta F_{ejkz}, \quad (22)$$

$$\Delta F_{ejkz} = k_i \Delta i_{jk} - k_z \Delta z_{gbjk}, \quad (23)$$

$$\Delta \dot{i}_{js} = \frac{k_z}{k_i} \Delta \dot{z}_{gbjs} - \frac{R_m}{L_o} \Delta i_{js} + \frac{1}{L_o} \Delta v_{js}, \quad (24)$$

where

$$F_{ejkzo} = \frac{\mu_o N_m^2 A_m i_o^2}{4 z_o^2}, \quad k_i = \frac{\mu_o N_m^2 A_m i_o}{2 z_o^2}, \quad k_z = \frac{\mu_o N_m^2 A_m i_o^2}{2 z_o^3}, \quad (25)$$

$$L_o = \frac{\mu_o N_m^2 A_m}{2 z_o}.$$

An explicit expression of \dot{z}_{gjs} including the vehicle speed V in Eqs. (21) and (24) is given in Sec. 3.1. On the other hand, for the case when the lateral guide force is not generated by an independent control system, the laterally controlled system can be idealized to be a virtual spring, of which the spring constant K_{ey} is determined as²⁸:

$$\Delta F_{ejky} = -K_{ey}\Delta y_{gbjk}, \quad K_{ey} = \frac{2F_{ejkzo}}{\pi w_m}. \quad (26)$$

Here, w_m = the width of the electromagnet; $\Delta y_{gbjk} = y_{bj} + H_b\theta_{bjx} + e_{kx}\theta_{bjz} - y_{rjk} - y_{gjk}$.

2.5. Control algorithm

While the maglev vehicle is levitated at a complete standstill, it should be stably supported by the electromagnetic force produced by a constant electromagnetic current. However, the running maglev vehicle can be destabilized by external disturbances such as wind force and surface irregularity. To stabilize the maglev floating system and secure its riding quality, it is important to select the appropriate active control algorithm. In this study, the UTM controller, which is used in the test maglev line in Korea, is applied and some selected output variables are measured by the installed sensors. The controller adopts the five-states feedback system to control the magnetic force. In this controller, the voltage is determined as follows:

$$\Delta v_{js} = k_1\Delta\ddot{z}_{gbjs} - k_1\hat{x}_{1js} + (-k_1V_1 + k_2)\hat{x}_{2js} + k_3\hat{x}_{3js} + (k_1V_1 + k_4)\hat{x}_{4js} + k_5\hat{x}_{5js}, \quad (27)$$

where $\hat{x}_{1js}, \hat{x}_{2js}, \hat{x}_{3js}, \hat{x}_{4js}, \hat{x}_{5js}$ = the estimated state vectors at the s th sensor of the j th bogie and k_1, k_2, k_3, k_4, k_5 and V_1 = the constants used in the control algorithm. The determined voltage has a decisive effect on the current in Eq. (24). The changed currents, which are supplied to each electromagnet, can cause variation in the fluctuating electromagnetic force to maintain the air gap within the permissible range. The UTM control algorithm can be expressed as follows:

$$\dot{\hat{\mathbf{x}}}_{js} = \mathbf{A}_s\hat{\mathbf{x}}_{js} + \mathbf{L}_s\mathbf{y}_{js}, \quad (28)$$

where $\hat{\mathbf{x}}_{js} = \{\hat{x}_{1js}, \hat{x}_{2js}, \hat{x}_{3js}, \hat{x}_{4js}, \hat{x}_{5js}\}^T$, $\mathbf{y}_{js} = \{\Delta\ddot{z}_{gbjs}, \Delta z_{gbjs}\}^T$

$$\mathbf{A}_s = \begin{bmatrix} 0 & 1/T_3 & 0 & -1/T_3 & 0 \\ -1/T_1 & -V_1/T_3 & 0 & V_1/T_1 & 0 \\ 0 & 1/T_2 & -V_2/T_2 & 0 & V_2/T_2 \\ 0 & 0 & 0 & -V_3/T_4 & -1/T_4 \\ 0 & 0 & 0 & 1/T_5 & 0 \end{bmatrix}, \quad \mathbf{L}_s = \begin{bmatrix} 0 & 0 \\ 1/T_1 & 0 \\ 0 & 0 \\ 0 & 1/T_4 \\ 0 & 0 \end{bmatrix}.$$

Here, T_1 to T_5 and V_1 to V_3 denote the constants used in the control algorithm and listed in Table 3; $\Delta\ddot{z}_{gbjs}$ and Δz_{gbjs} the measured acceleration and air-gap at the s th sensor of the j th bogie. Also, an explicit expression of \dot{z}_{gjs} in $\Delta\ddot{z}_{gbjs}$ is presented in Sec. 3.1.

Table 3. Properties of UTM control algorithm parameter.

Index	Specification	Index	Specification
k_1	33	T_3	0.3439
k_2	495	T_4	0.000242
k_3	0	T_5	0.022
k_4	26400	V_1	1.43
k_5	49500	V_2	1.1
T_1	0.22	V_3	0.22
T_2	0.011	—	—

3. Guideway Structure Model

In this section, the 3D equations of motion of a simply supported guideway are presented using the modal superposition method. In addition, a discussion is given on generation of the surface irregularity.

3.1. Modeling of a guideway girder

Generally, an attraction force exists between the electromagnet attached to the maglev vehicle and the reaction plate of the guideway to keep the vehicle levitated and to maintain an allowable air-gap. The forces generated from the EMS are transmitted directly to the guideway girder, which is assumed to be supported simply. Accordingly, the guideway structure shown in Fig. 5 can be modeled as a 3D simple beam.²⁴

Assuming that the guideway girder is subjected to only dynamic interaction forces existing between the vehicle and the guideway, the vertical, lateral, and torsional equations of motion of the girder can be expressed as

$$\rho_g A \ddot{w} + c_w \dot{w} + EI_y w'''' = \sum_{j=1}^{N_{\text{bogi}}} \sum_{k=1}^{N_{\text{ems}}} (F_{ejkzo} + \Delta F_{ejkz}) \delta(x - x_{jk}),$$

$$\rho_g A \ddot{v} + c_v \dot{v} + EI_z v'''' = \sum_{j=1}^{N_{\text{bogi}}} \sum_{k=1}^{N_{\text{ems}}} \Delta F_{ejky} \delta(x - x_{jk}),$$

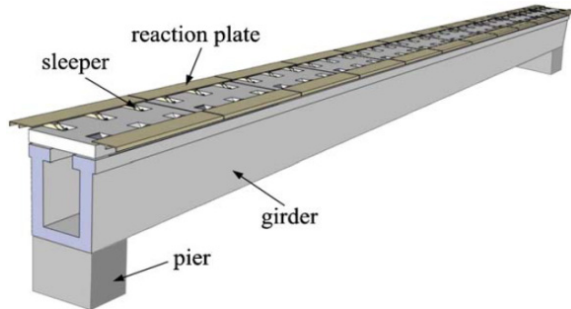


Fig. 5. Guideway girder.

$$\rho_g I_p \ddot{\theta} + c_\theta \dot{\theta} + GJ\theta'' = \sum_{j=1}^{N_{\text{bogj}}} \sum_{k=1}^{N_{\text{ems}}} [(F_{ejkzo} + \Delta F_{ejkz})e_{ky} - \Delta F_{ejky}H_g]\delta(x - x_{jk}), \quad (29)$$

where $F_{ejkzo} + \Delta F_{ejkz}$ and ΔF_{ejky} denote the vertical and lateral magnetic forces acting on the girder, respectively; and ρ_g = the density of the guideway; EI_y, EI_z , GJ = flexural rigidities with respect to the y and z axes and torsional rigidity; A = cross sectional area; I_p = polar moment of inertia; x_{jk} = position of the k th electromagnet of the j th bogie; H_g = height from the centroid of the guideway to the reaction plate; and w, v, θ = vertical, lateral, and torsional motions of the guideway, respectively.

Considering that the guideway is simply supported, the natural frequencies and the normalized mode-shapes corresponding to the vertical, lateral, and torsional deformations can easily be derived as

$$\begin{aligned} \omega_{zn} &= (n\pi)^2 \sqrt{\frac{EI_y}{\rho_g AL_b^4}} = 2\pi f_{zn}, & \phi_{zn} &= \sqrt{\frac{2}{\rho_g AL_b}} \sin\left(\frac{n\pi x}{L_b}\right), \\ \omega_{yn} &= (n\pi)^2 \sqrt{\frac{EI_z}{\rho_g AL_b^4}} = 2\pi f_{yn}, & \phi_{yn} &= \sqrt{\frac{2}{\rho_g AL_b}} \sin\left(\frac{n\pi x}{L_b}\right), \\ \omega_{\theta n} &= n\pi \sqrt{\frac{GJ}{\rho_g I_p L_b^2}} = 2\pi f_{\theta n}, & \phi_{\theta n} &= \sqrt{\frac{2}{\rho_g I_p L_b}} \sin\left(\frac{n\pi x}{L_b}\right). \end{aligned} \quad (30)$$

for $n = 1, 2, \dots$

Table 4 shows the geometric and material properties of the guideway girder model used, where the moment of inertia I_y is determined from the deflection ratio of 1/3000 due to the weight of one maglev vehicle. In addition, the last row sums up the vertical, lateral, and torsional natural frequencies of the simple beam evaluated based on the given data.

The modal superposition method that considers only the mode shapes of the girder is adopted to treat Eq. (30) more efficiently. The vertical, lateral and torsional

Table 4. Geometric and material properties of the guideway model.

Index	Values
Elastic modulus (E)	$3 \times 10^{10} \text{ N/m}^2$
Shear elastic modulus (G)	$1.5 \times 10^{10} \text{ N/m}^2$
Cross sectional area (A)	1.12 m^2
Area moments of inertia (I_y, I_z)	$0.471, 0.276 \text{ m}^4$
Polar moment of inertia (I_p)	0.747 m^4
Torsional constant (J)	0.514 m^4
Density of the girder (ρ_g)	3000 kg/m^3
Vertical, lateral, and torsional natural frequencies ($f_{zn}, f_{yn}, f_{\theta n}$)	$5.13 \text{ n}^2, 3.94 \text{ n}^2, 37.1 \text{ n Hz}$ for $n = 1, 2, \dots, 10$

displacements of the guideway can then be expressed as a finite summation of the multiplications of the mode shapes and corresponding generalized coordinates, respectively, as follows:

$$\begin{aligned} w(x, t) &= \sum_{n=1}^{10} q_{zn}(t) \phi_{zn}(x), \\ v(x, t) &= \sum_{n=1}^{10} q_{yn}(t) \phi_{yn}(x), \\ \theta(x, t) &= \sum_{n=1}^{10} q_{\theta n}(t) \phi_{\theta n}(x). \end{aligned} \quad (31)$$

To explicitly obtain the vertical velocity \dot{z}_{gjs} and acceleration \ddot{z}_{gjs} of the girder at the s th sensor position of the j th bogie in Eqs. (24) and (28), respectively, the vertical displacement z_{gjs} can be expressed as

$$z_{gjs}(t) = \sum_{n=1}^{10} q_{zn}(t) \phi_{zn}(x_{js}(t)) \quad (32a)$$

Considering the vehicle speed V , the vertical velocity and acceleration of the girder are derived using the chain rule as

$$\dot{z}_{gjs}(t) = \sum_{n=1}^{10} [\dot{q}_{zn}(t) \phi_{zn}(x_{js}) + V q_{zn}(t) \phi'_{zn}(x_{js})], \quad (32b)$$

$$\ddot{z}_{gjs}(t) = \sum_{n=1}^{10} [\ddot{q}_{zn}(t) \phi_{zn}(x_{js}) + 2V \dot{q}_{zn}(t) \phi'_{zn}(x_{js}) + V^2 q_{zn}(t) \phi''_{zn}(x_{js})]. \quad (32c)$$

Finally, considering the orthogonality property of the normal modes, the generalized equations of motion for the guideway are obtained from Eq. (29) as

$$\begin{aligned} \ddot{q}_{zn} + 2\xi_{zn}\omega_{zn}\dot{q}_{zn} + \omega_{zn}^2 q_{zn} &= \sum_{i=1}^{N_{\text{bogi}}} \sum_{k=1}^{N_{\text{ems}}} (F_{ejkzo} + \Delta F_{ejkz}) \phi_{zn}(x_{jk}), \\ \ddot{q}_{yn} + 2\xi_{yn}\omega_{yn}\dot{q}_{yn} + \omega_{yn}^2 q_{yn} &= \sum_{i=1}^{N_{\text{bogi}}} \sum_{k=1}^{N_{\text{ems}}} \Delta F_{ejky} \phi_{yn}(x_{jk}), \\ \ddot{q}_{\theta n} + 2\xi_{\theta n}\omega_{\theta n}\dot{q}_{\theta n} + \omega_{\theta n}^2 q_{\theta n} &= \sum_{i=1}^{N_{\text{bogi}}} \sum_{k=1}^{N_{\text{ems}}} [(F_{ejkzo} + \Delta F_{ejkz}) e_{ky} - \Delta F_{ejky} H_g] \phi_{\theta n}(x_{jk}), \end{aligned} \quad (33)$$

where ξ_{zn} , ξ_{yn} , and $\xi_{\theta n}$ = the damping ratios of vertical, lateral, and torsional motion, respectively, which are taken to be 0.02 in this study. Generally, the running vehicle can operate on the bridge or the ground. Hence, it should be noted that the corresponding mode shape $\phi(x_{jk})$ becomes zero when the magnet of the vehicle is located on the ground.

3.2. Surface irregularity

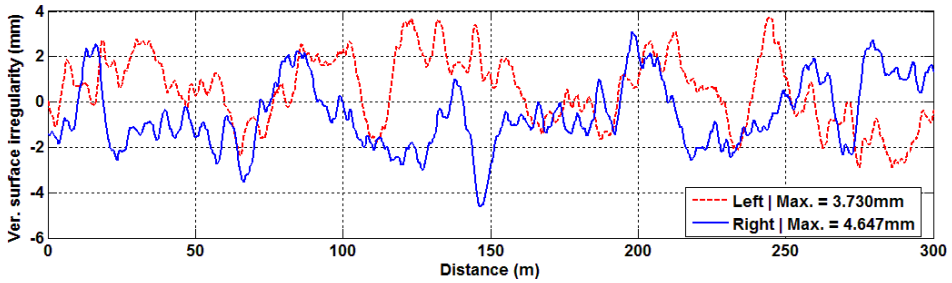
The irregularity of the reaction plates that correspond to the rails in a conventional railway is one of the main sources that induce vibrations on the vehicle and guideway structures. The geometry of the reaction plates is defined in terms of four irregularities consisting of gage, cross level, alignment, and vertical surface profile.²⁹ The surface irregularity is generally expressed as a power spectral density (PSD) function. Many types of PSD functions can be used for various surface transportation systems.^{28–31}

In this study, the 3D irregularity profiles of two parallel reaction plates (see Fig. 5) are independently generated, where the PSD proposed by the Federal Railroad Administration (FRA) is adopted for simulation. The vertical and lateral surface irregularity profiles of each reaction plate are numerically simulated using the following equations³²:

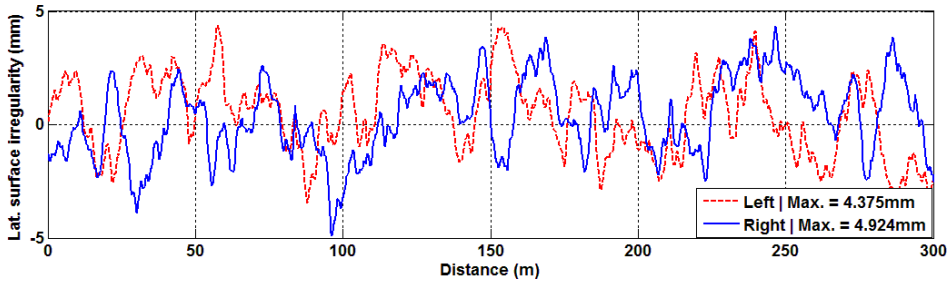
$$S_r(\Omega) = \frac{A\Omega_2^2}{(\Omega^2 + \Omega_1^2)(\Omega^2 + \Omega_2^2)}, \quad (34a)$$

$$w(x) = \sum_{i=1}^N \sqrt{2S_r(\Omega_i)\Delta\Omega} \cos(\Omega_i x - \theta_i), \quad (34b)$$

where $S_r(\Omega)$ = the PSD of surface irregularity; N = the number of the divided frequencies within the frequency bandwidth concerned; $\Delta\Omega$ = the frequency interval to



(a) Vertical surface irregularities of the right and left reaction plate.



(b) Lateral surface irregularities of the right and left reaction plate.

Fig. 6. Surface irregularity profiles generated from PSD function.

Table 5. Parameters for the PSD function by FRA.

Irregularity direction	Grade	A (m)	Ω_1 (m ⁻¹)	Ω_2 (m ⁻¹)
Vertical	3	2.16×10^{-8}	23.3×10^{-3}	13.1×10^{-2}
Lateral	3	3.15×10^{-8}	29.2×10^{-3}	23.3×10^{-2}

be 0.002 in this study; and θ_i = the independent random variables that are uniformly distributed from 0 to 2π .

Three types of roughness profiles are used for comparative simulation where the third grade (see Table 5) of 6 grades classified by FRA is chosen as the normal condition, and two times and half of the third grade are applied as a poor and good condition, respectively. In this study, the vertical and lateral profiles of the 3-grade (normal condition) along a 1000 m distance have been generated for surface irregularities of the right and left reaction plates, respectively. Figures 6(a) and 6(b) show only the profiles of the 300 m distance under the normal condition, in which the first 25 m is for a guideway girder of 25 m span length and the remaining 275 m for the ground. However, for the case where the guideway structure consists of 10 simple span girders, to investigate the resonance phenomena of one vehicle, the 250 m and 50 m distances are used for the guideways and the ground, respectively.

4. Coupled Dynamic Analysis of Maglev and Guideway System

An iterative analysis procedure of the coupled maglev system is first presented and the resonance conditions are then addressed considering the multi-vehicles or multi-guideways.

4.1. Dynamic interaction analysis for the coupled system

Basically, a maglev vehicle model running on a simply supported girder is considered as shown in Fig. 7. Such a coupled system will be solved by iterative Newmark method to yield the time history response. In order to explain the iterative analysis procedure efficiently, an iterative interaction algorithm for solving the coupled equations of one vehicle and one guideway is first presented, which is then extended to the cases of a series of vehicles or multi-guideways.

The equations of motion of a maglev vehicle have been derived in Sec. 2 with consideration of Eqs. (5)–(9), Eqs. (13)–(17), Eq. (24), and Eq. (28). Taking into account the variable numbers of one cabin (5), four bogies (20), currents (16) at four sensors per bogie, and state vectors (80), the matrix equation of the vehicle at time t

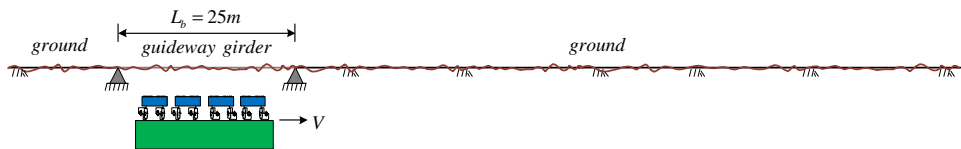


Fig. 7. Maglev vehicle running on a simply supported girder.

can be expressed as

$$\mathbf{M}_v \ddot{\mathbf{x}}_v + \mathbf{C}_v \dot{\mathbf{x}}_v + \mathbf{K}_v \mathbf{x}_v = \mathbf{f}_v(\Delta F_{ejkz}, \Delta F_{ejky}), \quad (35a)$$

where \mathbf{M}_v , \mathbf{C}_v , \mathbf{K}_v = the 121×121 mass, damping, and stiffness matrices of the maglev vehicle;

$$\mathbf{x}_v^T = \left\{ \underbrace{y_c z_c \theta_{cx} \theta_{cy} \theta_{cz}}_{\text{cabin}(5)} \underbrace{y_{b1} \cdots \theta_{b4y} \theta_{b4z}}_{\text{bogies}(5 \times 4)} \underbrace{i_{11} i_{12} \cdots i_{44}}_{\text{currents}(4 \times 4)} \underbrace{\hat{x}_{111} \hat{x}_{211} \hat{x}_{311} \cdots \hat{x}_{444} \hat{x}_{544}}_{\text{statevectors}(5 \times 16)} \right\}_{121 \times 1}.$$

Also, the equations of motion of a guideway structure under a moving self-weight \mathbf{f}_{vo} have been presented based on the modal superposition method in Sec. 3, i.e.

$$\mathbf{M}_g \ddot{\mathbf{x}}_g + \mathbf{C}_g \dot{\mathbf{x}}_g + \mathbf{K}_g \mathbf{x}_g = \mathbf{f}_g(\Delta F_{ejkz}, \Delta F_{ejky}) + \mathbf{f}_{vo}, \quad (35b)$$

where

$$\mathbf{x}_g^T = \{q_{z1} q_{z2} q_{z3} \cdots q_{zn}; q_{y1} \cdots q_{yn}; q_{\theta 1} \cdots q_{\theta n}\},$$

$$\mathbf{M}_g = \mathbf{I}_n, \quad n = zn + yn + \theta n,$$

$$\mathbf{C}_g = 2\text{diag}[\xi_1 \omega_1 \xi_2 \omega_2 \cdots \xi_n \omega_n],$$

$$\mathbf{K}_g = \text{diag}[\omega_1^2 \omega_2^2 \cdots \omega_n^2].$$

In addition, the size of the system matrices regarding the guideway girder becomes 30×30 because 10 modes each in the vertical, lateral, and torsional directions, respectively, are chosen in this study. Also, the subscripts “v” and “g” refer to the vehicle and guideway, respectively.

For comparison, for the case of the 2D maglev system, the total variable numbers of the maglev and the guideway models are reduced to 58 and 10, respectively. Accordingly, neglecting the guidance forces, the matrix equations of motion for a vehicle and a guideway in the 2D system can be expressed as follows:

$$\mathbf{M}_v \ddot{\mathbf{x}}_v + \mathbf{C}_v \dot{\mathbf{x}}_v + \mathbf{K}_v \mathbf{x}_v = \mathbf{f}_v(\Delta F_{ejkz}), \quad (36a)$$

$$\mathbf{M}_g \ddot{\mathbf{x}}_g + \mathbf{C}_g \dot{\mathbf{x}}_g + \mathbf{K}_g \mathbf{x}_g = \mathbf{f}_g(\Delta F_{ejkz}) + \mathbf{f}_{vo}, \quad (36b)$$

where $\mathbf{x}_g^T = \{q_{z1} q_{z2} q_{z3} \cdots q_{zn}\}$

$$\mathbf{x}_v^T = \left\{ \underbrace{z_c \theta_{cy}}_{\text{cabin}(2)} \underbrace{z_{b1} \cdots \theta_{b4y}}_{\text{bogies}(2 \times 4)} \underbrace{i_{11} i_{12} \cdots i_{42}}_{\text{currents}(2 \times 4)} \underbrace{\hat{x}_{111} \hat{x}_{211} \hat{x}_{311} \cdots \hat{x}_{442} \hat{x}_{542}}_{\text{statevectors}(5 \times 8)} \right\}_{58 \times 1}.$$

As mentioned previously, the coupled equations of Eq. (35a) are connected through the interaction forces \mathbf{f}_g and \mathbf{f}_v due to the electromagnetic forces ΔF_{ejkz} and ΔF_{ejky} , which are functions of relative displacements, velocities, and currents between them at the position of the maglev running on the guideway at time t . However, it should be realized that these state variables are not known in advance. In this study, an *iterative* analysis procedure based on the Newmark method is adopted to solve the coupled equations.

By Newmark's procedure, a simultaneous equation with respect to $\mathbf{x}_v^{(k+1)}$ can be obtained from Eq. (35a) for time $t + \Delta t$ as follows:

$$(\mathbf{K}_v + a_o \mathbf{M}_v + a_1 \mathbf{C}_v) \mathbf{x}_v^{(k+1)} = \mathbf{f}_v(\Delta F_{ejkz}^{(k)}, \Delta F_{ejky}^{(k)}) + \mathbf{M}_v(a_o \hat{\mathbf{x}}_v + a_2 \hat{\mathbf{x}}_v + a_3 \hat{\mathbf{x}}_v) + \mathbf{C}_v(a_1 \hat{\mathbf{x}}_v + a_4 \hat{\mathbf{x}}_v + a_5 \hat{\mathbf{x}}_v), \quad (37)$$

where a_o to a_5 are constants, and the interaction forces $\Delta F_{ejkz}^{(k)}, \Delta F_{ejky}^{(k)}$ are determined from the responses of the previous iteration step as

$$\begin{aligned} \Delta F_{ejkz}^{(k)} &= k_i \Delta i_{jk}^{(k)} - k_z(z_{bj}^{(k)} - e_{kx} \theta_{bjy}^{(k)} + e_{ky} \theta_{bjx}^{(k)} - z_{rjk} - z_{gjk}^{(k)}), \\ \Delta F_{ejky}^{(k)} &= -K_{ey}(y_{bj}^{(k)} + H_b \theta_{bjx}^{(k)} + e_{kx} \theta_{bjz}^{(k)} - y_{rjk} - y_{gjk}^{(k)}). \end{aligned} \quad (38)$$

Similar to Eq. (35a), the equations of motion for the guideway girder, Eq. (35b), are transformed to

$$\begin{aligned} (\mathbf{K}_g + a_o \mathbf{M}_g + a_1 \mathbf{C}_g) \mathbf{x}_g^{(k+1)} &= \mathbf{f}_g(\Delta F_{ejkz}^{(k+1)}, \Delta F_{ejky}^{(k+1)}) + \mathbf{f}_{vo} + \mathbf{M}_g(a_o \hat{\mathbf{x}}_g + a_2 \hat{\mathbf{x}}_g + a_3 \hat{\mathbf{x}}_g) \\ &+ \mathbf{C}_g(a_1 \hat{\mathbf{x}}_g + a_4 \hat{\mathbf{x}}_g + a_5 \hat{\mathbf{x}}_g), \end{aligned} \quad (39)$$

where

$$\begin{aligned} \Delta F_{ejkz}^{(k+1)} &= k_i \Delta i_{jk}^{(k+1)} - k_z(z_{bj}^{(k+1)} - e_{kx} \theta_{bjy}^{(k+1)} + e_{ky} \theta_{bjx}^{(k+1)} - z_{rjk} - z_{gjk}^{(k)}), \\ \Delta F_{ejky}^{(k+1)} &= -K_{ey}(y_{bj}^{(k+1)} + H_b \theta_{bjx}^{(k+1)} + e_{kx} \theta_{bjz}^{(k+1)} - y_{rjk} - y_{gjk}^{(k)}). \end{aligned} \quad (40)$$

Furthermore, it should be noted that $\Delta F_{ejkz}^{(k+1)}, \Delta F_{ejky}^{(k+1)}$ are calculated using the responses of the girder in the previous iteration step and the updated responses of the vehicle due to the solution to Eq. (37).

Based on Eqs. (37)–(40), the flow chart of Fig. 8 shows the predictor–corrector iteration algorithm implemented in this study.

In order to analyze the resonant vibrations of the coupled system under various situations, a series of vehicles running on one guideway girder or a single vehicle on multi-girders are considered as shown in Fig. 9. For the case where a sequence of maglev vehicles travels over a bridge girder (Fig. 9(a)), even though the equations of motion for a guideway girder remain unchanged, the vehicle system matrices for the N_v vehicles should be expanded as follows:

$$\begin{aligned} \mathbf{M}_v &= \text{diag}[\mathbf{M}_v^1; \mathbf{M}_v^2; \mathbf{M}_v^3 \cdots \mathbf{M}_v^{N_v}], \\ \mathbf{C}_v &= \text{diag}[\mathbf{C}_v^1; \mathbf{C}_v^2; \mathbf{C}_v^3 \cdots \mathbf{C}_v^{N_v}], \\ \mathbf{K}_v &= \text{diag}[\mathbf{K}_v^1; \mathbf{K}_v^2; \mathbf{K}_v^3 \cdots \mathbf{K}_v^{N_v}], \\ \mathbf{x}_v^T &= \{\mathbf{x}_v^1; \mathbf{x}_v^2; \mathbf{x}_v^3 \cdots \mathbf{x}_v^{N_v}\}, \\ \mathbf{f}_v^T &= \{\mathbf{f}_v^1 + \mathbf{f}_w^1; \mathbf{f}_v^2 + \mathbf{f}_w^2 \cdots \mathbf{f}_v^{N_v} + \mathbf{f}_w^{N_v}\}. \end{aligned} \quad (41)$$

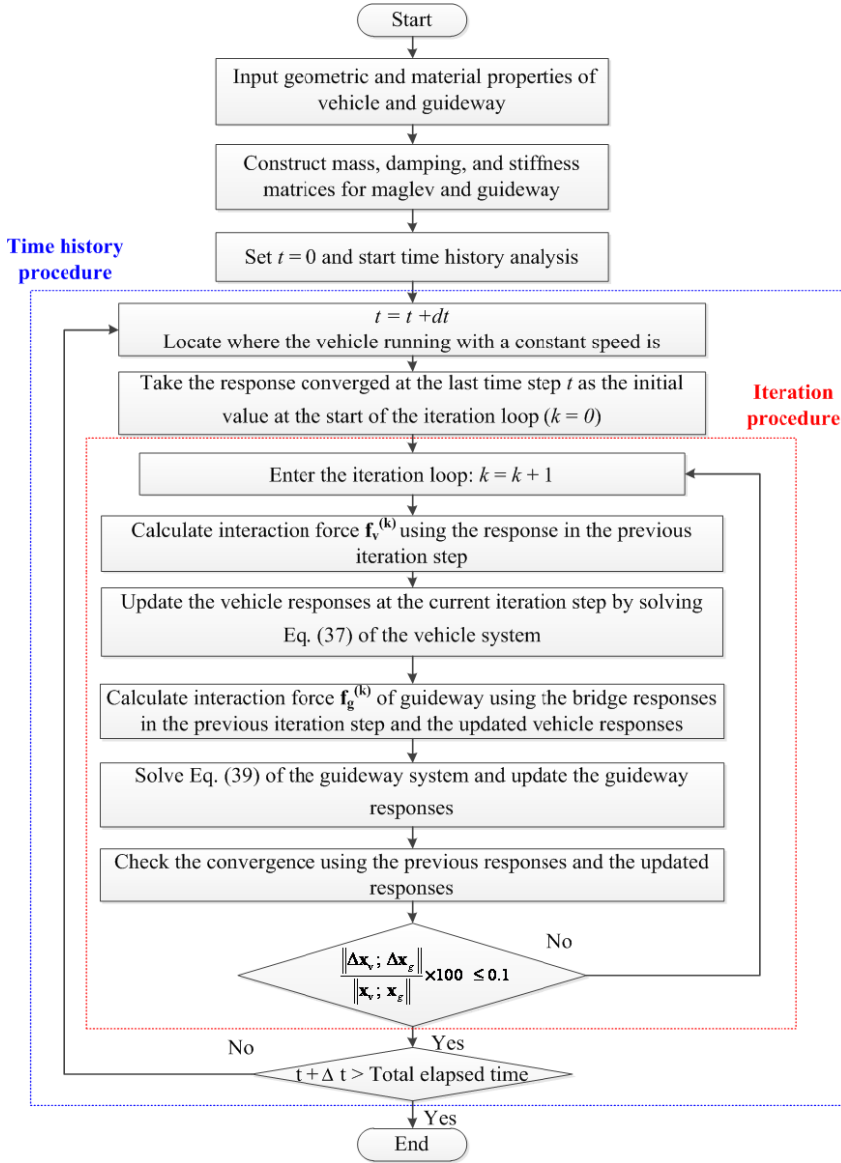


Fig. 8. Flow chart of a dynamic interaction analysis procedure with an iterative loop.

On the other hand, for the case where a vehicle runs over a series of N_g simple girders (Fig. 9(b)), the girder system matrices similarly need to be constructed for multi-guideways. To investigate the resonant behaviors of the vehicle, we consider only the scenarios of a vehicle running over one simple girder or at most two girders. Accordingly, the system matrices of one or two girders depending on the current position of the vehicle are made for efficient calculation.

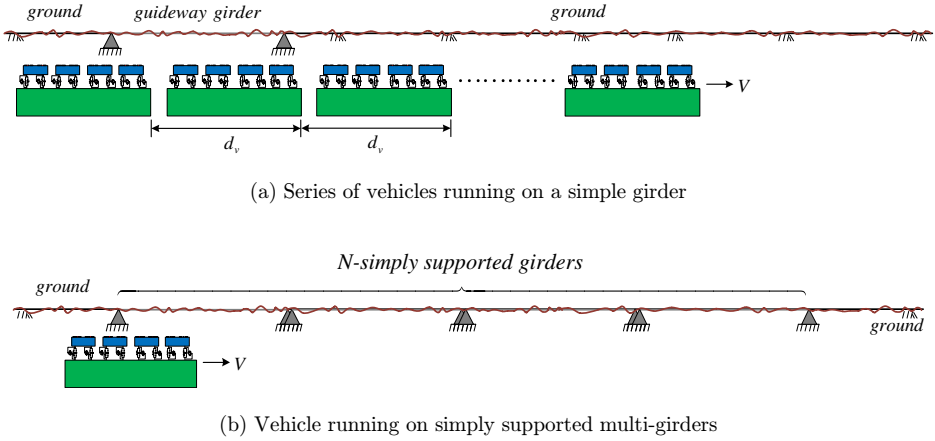


Fig. 9. Maglev vehicle systems running on guideway girder and ground sections.

4.2. Resonance conditions

When a series of equidistant moving vehicles run over several bridges with the same span length at a certain speed, resonant vibrations can be induced on the bridge or vehicle, and that certain speed is called the resonance speed. The resonance phenomena of a vehicle-bridge system are important factors effecting the dynamic responses. Thus, the resonance condition should be carefully examined when a row of trains move over a bridge.

Research work on this subject has been conducted by many scholars. Particularly, Yang *et al.*³³ identified the resonance and its cancellation conditions for the waves generated by continuously moving loads on a simple beam using an analytical approach, Xia *et al.*³⁴ investigated the resonance conditions of a train-bridge system through theoretical derivations, numerical simulations, and experimental data analyses, and Xu *et al.*³⁵ discussed the resonance conditions of a simple beam under a sequence of equidistant moving loads and an extension to a continuous beam sitting on an elastic foundation. Also, Wang *et al.*³⁶ investigated the resonance and sub-resonance phenomena of a two-span continuous railway bridge under the passage of moving train loadings.

In this section, the resonance conditions on the bridge girder or vehicle are presented based on various previous works.^{34–36}

To derive the resonant vibration condition of the girder, we consider a sequence of moving loads traveling on a bridge girder as shown in Fig. 10. For simplicity, each

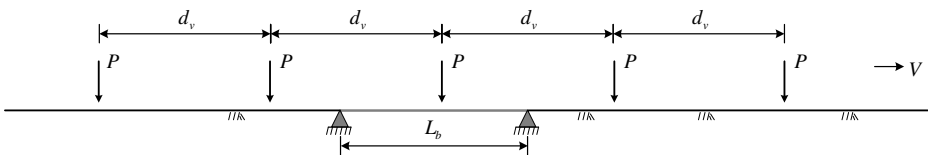


Fig. 10. Series of concentrated forces moving on a bridge.

vehicle load is regarded as a concentrated self-weight p moving on the guideway at a constant speed V . Let the interval of the moving loads be d_v . The equation of the vertical motion can be expressed as

$$\rho A \ddot{w} + EI_y w'''' = p \sum_{k=0}^{N-1} \delta \left[x - V \left(t - \frac{k d_v}{V} \right) \right] \times \left[H \left(t - \frac{k d_v}{V} \right) - H \left(t - \frac{k d_v}{V} - \frac{L_b}{V} \right) \right]. \quad (42)$$

Introducing $w(x, t) = \sum q_n(t) \sin \frac{n\pi x}{L}$, the n th modal equation of Eq. (42) and its particular solution, respectively, can be derived as

$$\begin{aligned} \ddot{q}_{zn} + \omega_{zn}^2 q_{zn} &= \frac{2p}{\rho A L_b} \sum_{k=1}^{N-1} \sin \frac{n\pi V}{L_b} \left(t - \frac{k d_v}{V} \right) \\ &\times \left[H \left(t - \frac{k d_v}{V} \right) - H \left(t - \frac{k d_v}{V} - \frac{L_b}{V} \right) \right], \\ q_{zn}(t) &= \frac{2p}{\rho A \omega_{zn}^2 L_b} \frac{1}{1 - \beta_{zn}^2} \\ &\times \sum_{k=0}^{N-1} \left[\Lambda \left(t - \frac{k d_v}{V} \right) + (-1)^{n+1} \Lambda \left(t - \frac{k d_v}{V} - \frac{L_b}{V} \right) \right], \end{aligned} \quad (43)$$

where

$$\begin{aligned} \Lambda(t) &= [\sin \bar{\omega}_n t - \beta_{zn} \sin \omega_{zn} t] H(t), \quad \bar{\omega}_n = \frac{n\pi V}{L_b}, \\ \omega_{zn} &= (n\pi)^2 \sqrt{\frac{EI_y}{\rho A L_b^4}} = 2\pi f_{zn}, \quad \beta_{zn} = \frac{\bar{\omega}_n}{\omega_{zn}}. \end{aligned}$$

It is noted that the vertical response of the beam is excited to the utmost, as all the first $N - 1$ moving loads pass the beam. The resonance condition can be derived using Eq. (43) as follows³³:

$$V = \frac{f_{z1} d_v}{i} \quad \text{for } i = 1, 2, 3, \dots \quad (44)$$

Also, the condition of cancellation is³³:

$$\frac{L_b}{d_v} = i - 0.5 \quad \text{for } i = 1, 2, 3, \dots \quad (45)$$

Generalizing Eq. (44) into the condition for higher frequencies and converting the unit in m/s to that in km/h, the resonance condition for vertical motions of a bridge girder by a sequence of moving vehicles can then be obtained as follows:

$$V_{br} = \frac{3.6 f_{zn} d_v}{i} \quad \text{for } n = 1, 2, \dots; i = 1, 2, \dots, \quad (46)$$

where the unit of V_{vr} is km/h. The preceding equation implies that for a series of loads moving on a bridge with a constant speed V_{br} , there exists a loading period d_v/V_{br} , which can cause resonance on the bridge when it approaches the period of the girder. However, it should be noted that resonance will not occur at the resonance speed if both Eqs. (46) and (45) are met simultaneously. In addition, the resonance speeds corresponding to i more than 1 in Eq. (46) are known as the sub-resonance condition.

On the other hand, the equation of motion due to the lateral roughness y_r is

$$\begin{aligned} \rho A \ddot{v} + EI_z v'''' = & \sum_{k=1}^{N-1} K_{ey} y_r(x) \delta \left[x - V \left(t - \frac{k d_v}{V} \right) \right] \\ & \times \left[H \left(t - \frac{k d_v}{V} \right) - H \left(t - \frac{k d_v}{V} - \frac{L_b}{V} \right) \right]. \end{aligned} \quad (47)$$

Taking an average of the roughness function over the bridge section approximately leads to the following equation:

$$\begin{aligned} \rho A \ddot{v} + EI_z v'''' = & K_{ey} \bar{y}_r \sum_{k=1}^{N-1} \delta \left[x - V \left(t - \frac{k d_v}{V} \right) \right] \\ & \times \left[H \left(t - \frac{k d_v}{V} \right) - H \left(t - \frac{k d_v}{V} - \frac{L_b}{V} \right) \right], \end{aligned} \quad (48)$$

where $\bar{y}_r \equiv \frac{1}{L_b} \int_0^{L_b} y_r dx$. Regarding $K_{ey} \bar{y}_r$ as p in the preceding equation, it can be observed that Eq. (46) serves as a lateral resonance condition if f_{yn} is inserted instead of f_{zn} , even though the response in the lateral resonance is not expected to be large because $K_{ey} \bar{y}_r$ is very small.

The resonance condition incurring resonant vibration of a vehicle running on simply supported multiple girders is then taken into account. In this case, the vertical resonance speed V_{vr} of the vehicle³⁴ is determined from the condition whereby the fundamental frequency of the vehicle f_v is equal to the load frequency V_{vr}/L_b as follows:

$$V_{vr} = 3.6 f_v L_b. \quad (49)$$

Recently, Yang and Yau³⁷ showed that the *pitching* resonance can occur for a vehicle passing over a series of simple beams, for which the *pitching* resonance speed $V_{pr}(= 3.6 f_p L_b)$ can be determined by simply substituting the pitching frequency f_p of the vehicle for f_v into Eq. (49).

5. Numerical Examples

Numerical examples are presented to simulate the coupling behaviors of the present 2D and 3D maglev-guideway models to evaluate their feasibility. Geometric and material properties in terms of the maglev vehicle model are given in Tables 1–3, in which the vehicle is assumed to be full of passengers. Also, the guideway girder model

is assumed to be a simply supported beam with a deflection ratio of 3000 and its properties are listed in Table 4. Ten vertical mode shapes are used in the 2D model and 30 mode shapes, including 10 modes for the lateral and torsional vibrations, are used in the 3D model. Basically, normal irregularity condition is considered in both the 2D and 3D analysis and the vertical and lateral irregularity profiles are generated separately for the left and right rails in the 3D analysis as shown in Fig. 6. In addition, the time interval Δt of 0.0005 s and the initial air-gap z_o of 8 mm are used.

Basically, the vehicle is excited a few seconds by the prescribed roughness of the ground to give an initial disturbance to the maglev vehicle before entering the guideway girder as shown in Fig. 7. The analyses in Secs. 5.1 and 5.2 are performed for the case where one maglev vehicle moves over one bridge section with a span length of 25 m and on the ground section of 275 m with poor, normal, and good roughness conditions. Particularly, in Secs. 5.3 and 5.4, the interaction systems consisting of 10 vehicles with the interval d_v of 12.1 and 24.2 m and one girder with normal roughness condition are analyzed to explore the vertical and lateral resonance conditions of the girder. Also, in Sec. 5.5, a system consisting of one vehicle and 10 girders with normal roughness is considered to examine when the vehicle vibrates resonantly.

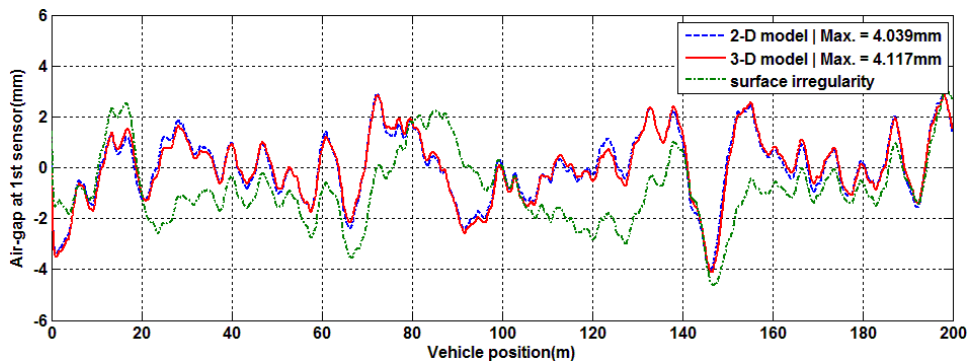
5.1. Comparison of simulation results using 2-D and 3-D maglev-guideway models

Time history analyses are performed for the 2D and 3D maglev systems consisting of a vehicle and a girder at the speed of 300 km/h. The results obtained for two systems are compared in this section. Figure 11 shows the time history responses for the vertical air-gap at the first sensor, the vertical acceleration at the center of the cabin, the current at the first sensor, vertical displacement, bending moment, and the vertical acceleration at the center of the girder, in which “static” refers to the results obtained by the static analysis under the moving maglev load and “vehicle position” denotes the current position of the first sensor attached at the first bogie of the maglev train.

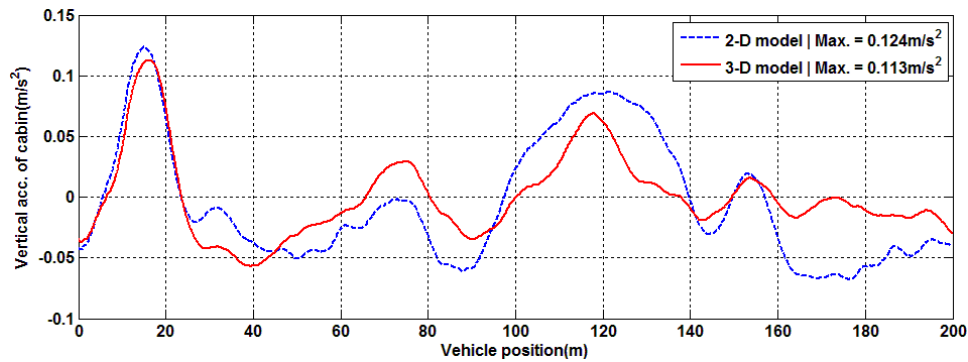
It is observed from Fig. 11 that the overall responses of the 2D and 3D vehicle and girder models are quite similar along the distance of simulation, and that the responses of the girder in Figs. 11(d)–11(f) are nearly identical. This means that the girder responses are much more insensitive to roughness profiles with high frequencies than the vehicle responses. In addition, it is noted that the girder responses shown in Fig. 11 become conspicuously large over the girder section of about 30 m due to the direct impact effects of one vehicle. Also, the impact factors of vertical displacement and bending moment at the center of the girder by the 3D model are calculated as 0.25 and 0.25, respectively.

5.2. Effects of surface irregularity and vehicle speed

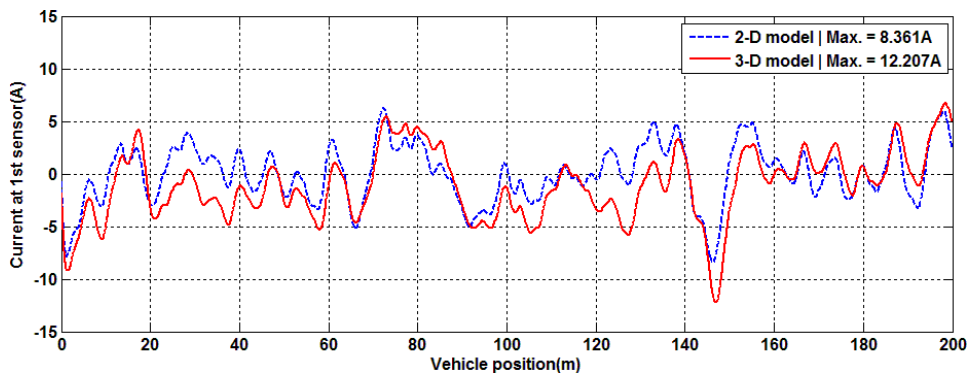
In this section, the effects of surface irregularity on dynamic response are examined by applying “poor”, “normal”, and “good” roughness conditions to the 2D and 3D



(a) Vertical air-gap at first sensor.

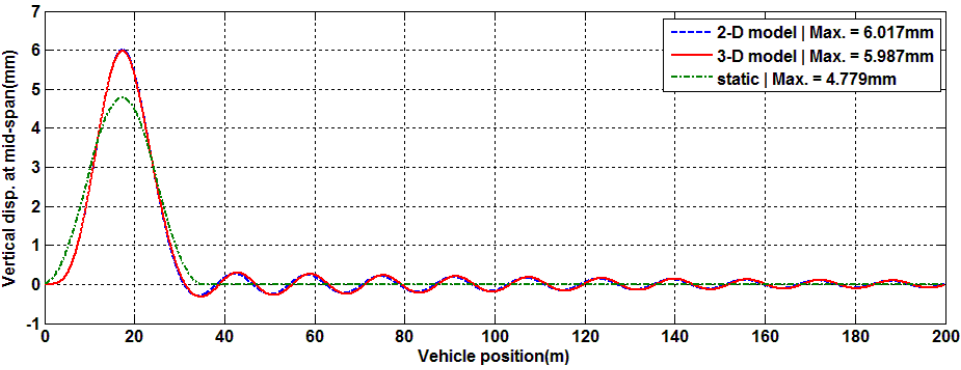


(b) Vertical acceleration at center of cabin.

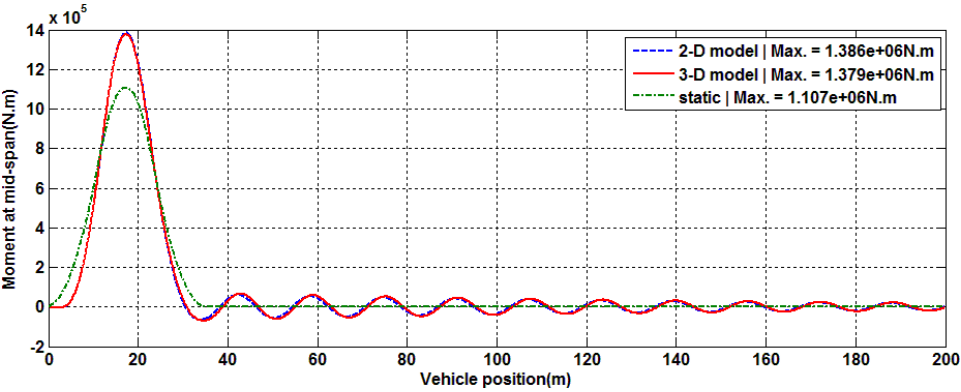


(c) Fluctuating current at first sensor.

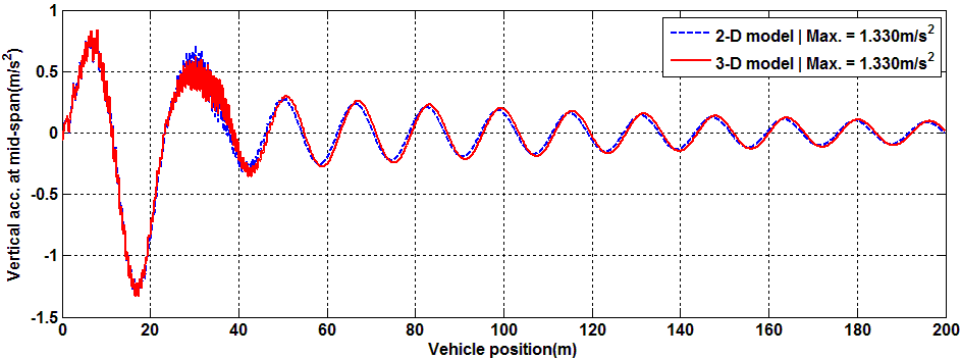
Fig. 11. Time history responses of 2-D and 3-D systems consisting of a vehicle and a girder.



(d) Vertical displacement at mid-span.

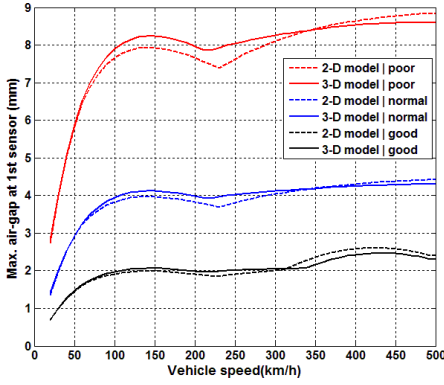


(e) Bending moment at mid-span.

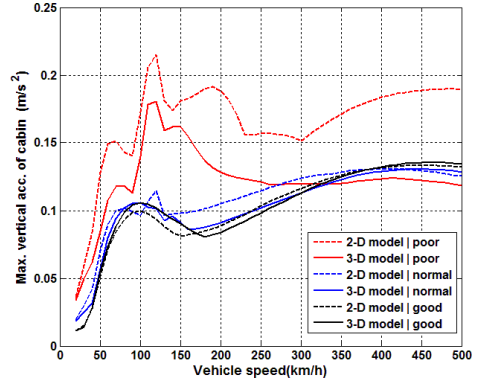


(f) Vertical acceleration at mid-span.

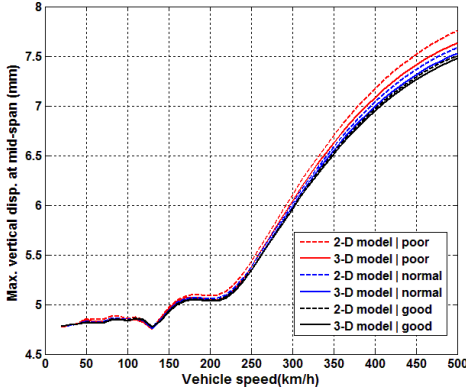
Fig. 11. (Continued)



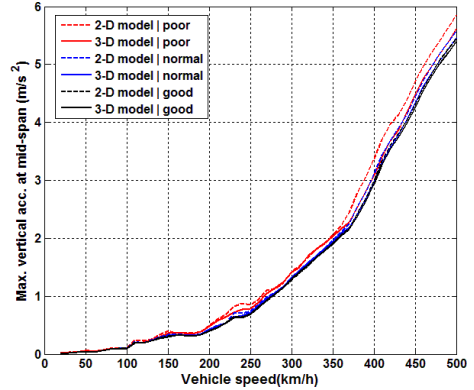
(a) Vertical air-gap at first sensor.



(b) Vertical acceleration at center of cabin.



(c) Vertical displacement at mid-span.



(d) Vertical acceleration at mid-span.

Fig. 12. Maximum responses for various irregularities versus vehicle speed.

models and increasing the vehicle speed from 20 to 500 km/h. Figure 12 shows the maximum responses of the vertical air-gap at the first sensor, acceleration at the center of the cabin, vertical displacement, and acceleration at the mid-span, respectively, with the increase of vehicle speed. From Figs. 12(a) and 12(b), we observe that the fluctuating air-gap and cabin acceleration are sensitively influenced by the surface irregularity and they increase rapidly up to the vehicle speed of 100 km/h, but do not change significantly at speeds higher than 100 km/h.

In addition, it is observed that acceleration responses of the cabin in the 3D maglev system are smaller than those in the 2D model. On the other hand, as shown in Figs. 12(c) and 12(d), the increasing rate of guideway responses is relatively small at vehicle speeds less than 200 km/h, but increases rapidly for speeds higher than 200 km/h. Furthermore, it can be seen that in contrast to vehicles, the girder responses by the dynamic interaction analysis are hardly influenced by surface irregularity.

5.3. Vertical resonance of a guideway girder under a series of vehicles

The vertically resonant behaviors of a single guideway girder under a series of 10 vehicles are investigated for d_v of 12.1 and 24.2 m to denote the intervals of equidistant moving vehicles. In this case, 10 vehicles will hit the girder repeatedly over the range of about 140 to 260 m depending on the magnitude of d_v and the impact released by the vehicles will exert some reverse influence on the girder as the last vehicle leaves.

5.3.1. Vertical resonance of a girder under a series of 10 vehicles

Figures 13(a) and 13(b) and Figs. 13(c) and 13(d) show the time history responses of the vertical displacement and acceleration at the mid-span when 10 vehicles have passed on the guideway with the vehicle speeds of 230, 300 km/h for $d_v = 12.1$ m and 450, 500 km/h for $d_v = 24.2$ m, respectively. Here, the predicted resonance speeds are calculated as 223.5 km/h ($= 3.6 \times 5.13 \times 12.1$) and 447.0 km/h ($= 3.6 \times 5.13 \times 24.2$), respectively, from the resonance condition of Eq. (46).

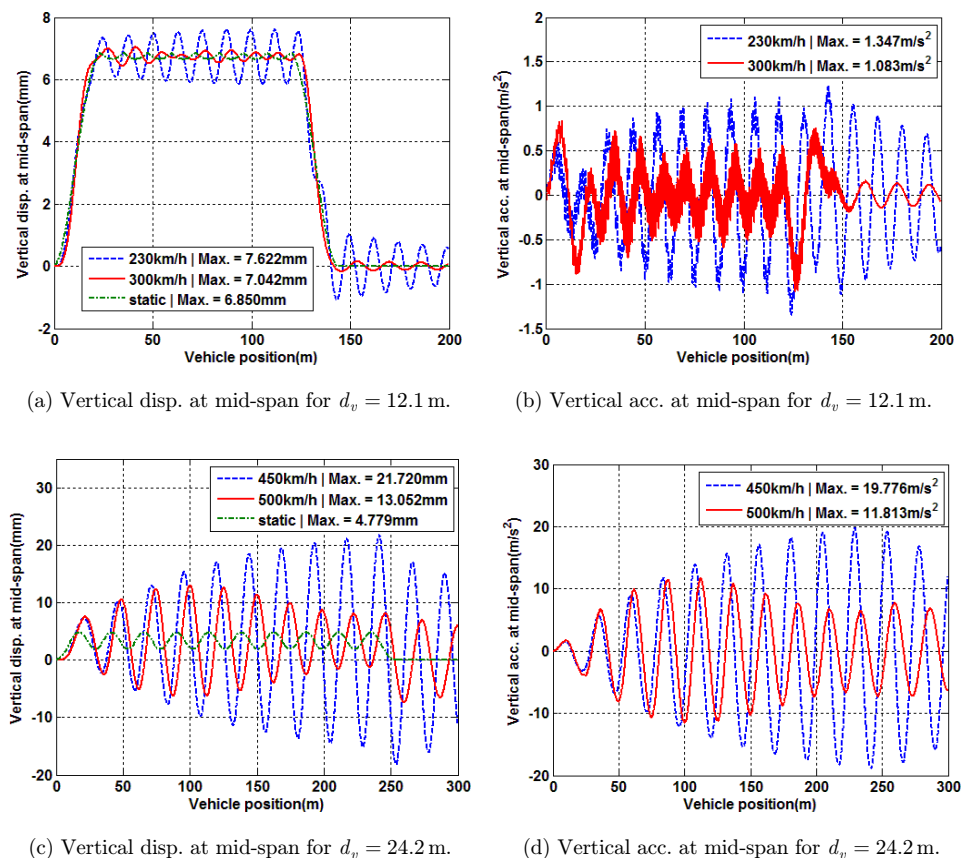


Fig. 13. Time history responses at center of girder at around resonance speeds.

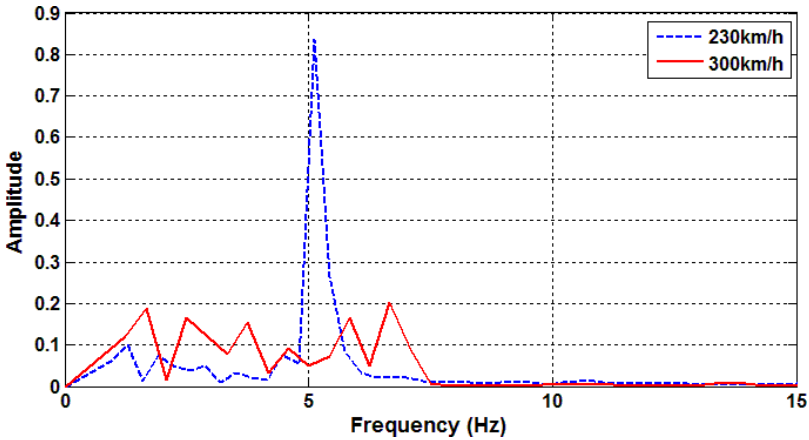
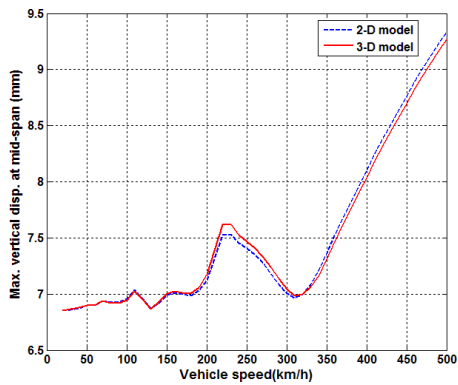


Fig. 14. Spectrum of accelerations of the center span at speeds of 230 and 300 km/h.

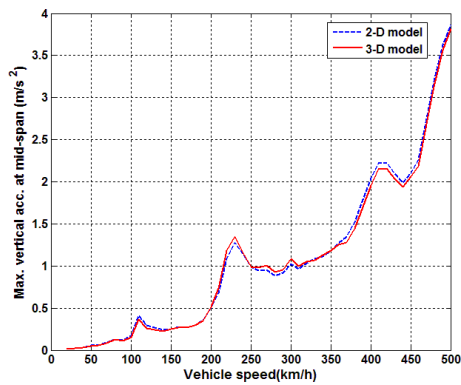
From Fig. 13, it is clear that the guideway response continues to increase linearly around the resonance speeds of 230 and 450 km/h, while resonant vibrations do not occur for 300 and 500 km/h. Particularly, both the displacement and acceleration finally increase significantly for the speed of 450 km/h for $d_v = 24.2$ m as each vehicle passes over the girder. Also, from the spectra of vertical acceleration in Fig. 14, a prominent peak near 5 Hz is detected for vehicle speed of 230 km/h.

In order to examine the validity of the resonance speeds of Eq. (46), time history analyses are conducted in the case of $d_v = 12.1$ m as the vehicle speed increases to 500 km/h. Figure 15 displays the maximum vertical displacements and accelerations at the center and 1/4 point of the guideway girder with an increase of the vehicle speed, respectively. Figure 15 shows that vertical resonance phenomenon occurs at around the first resonance speed of 223 km/h, its half speed of 111.7 km/h, and a fifth of the third resonance speed of 402.3 km/h ($= 223.5 \times 3^2/5$). Particularly, it should be noted that a local peak of around 178.8 km/h ($= 223.5 \times 2^2/5$) is observed in Fig. 15(d) only, which corresponds to a fifth of the second resonance speed. Moreover, the local peak cannot be found in Figs. 15(a) and 15(b) because the midpoint of the girder forms a node in its second mode shape. To supplement this, time history analysis is executed at a fifth of the second resonance speed, 178.8 km/h, and the vertical displacement and acceleration at a 1/4 point of the girder are plotted in Fig. 16. It is observed in Fig. 16 that the acceleration increases very gradually, although the displacement remains constant. In addition, Fig. 17 shows the variation of the maximum girder response with the vehicle speed for $d_v = 24.2$ m. A conspicuous peak of maximum responses is detected around the first resonance speed of 447 km/h.

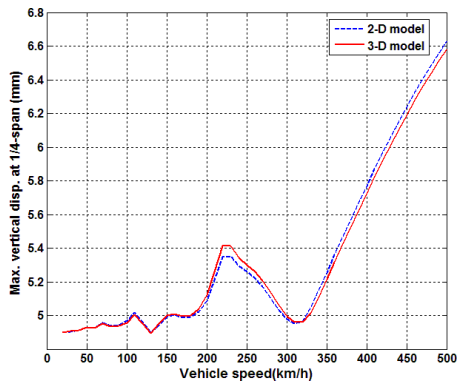
On the other hand, Fig. 18 shows the time history results obtained for different damping ratios of the guideway. From this figure, the resonance phenomenon is more clearly observed at the lower damping ratio. Therefore, it is concluded that the



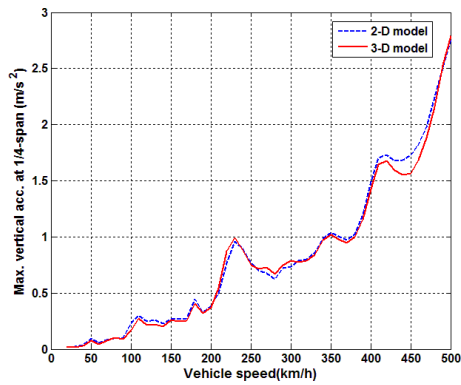
(a) Max. vertical disp. at mid-span.



(b) Max. vertical acc. at mid-span.

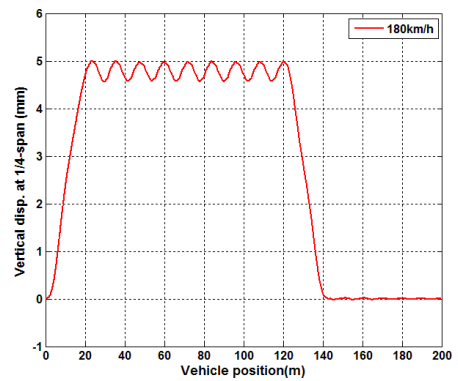


(c) Max. vertical disp. at 1/4 point of girder.

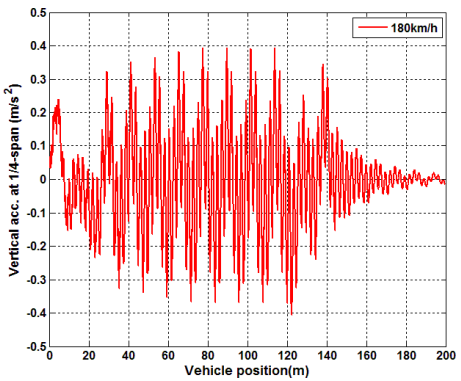


(d) Max. vertical acc. at 1/4 point of girder.

Fig. 15. Maximum responses at 1/2 and 1/4 point of girder versus vehicle speed for $d_v = 12.1$ m.



(a) Vertical disp. at 1/4 point of girder.



(b) Vertical acc. at 1/4 point of girder.

Fig. 16. Time history responses at a fifth of the second resonance speed, 178.8 km/h.

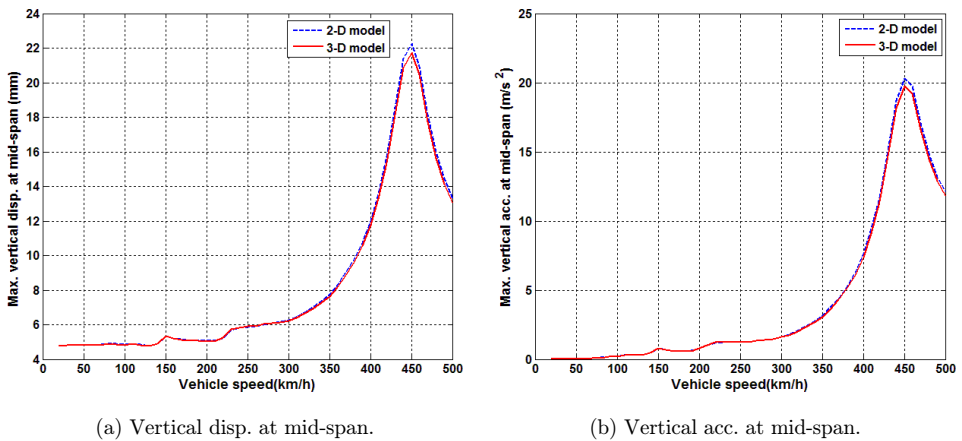


Fig. 17. Maximum responses at 1/2 of girder versus vehicle speed for $d_v = 24.2$ m.

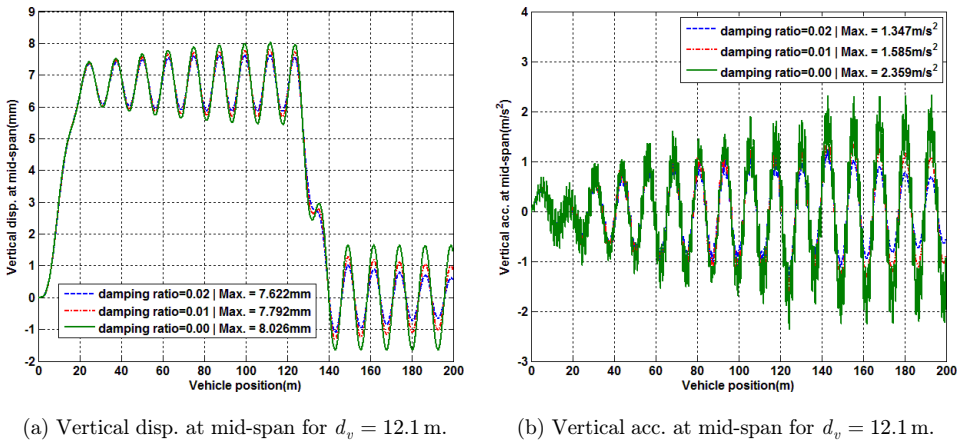


Fig. 18. Resonance of guideway for different damping ratios at 230 km/h.

simply supported girder with lower damping ratio is at risk for inducing significantly resonant vibrations in the girder, when a series of equidistant maglev vehicle runs at the first resonance speed.

Also of interest, Fig. 19 shows that the vertical accelerations at the center of the cabins of the first and the last vehicle have speeds of 450 and 500 km/h, respectively. The acceleration of the 10th cabin with 450 km/h is drastically larger than its acceleration with 500 km/h when it passes the guideway girder, while the acceleration of the first cabin at 450 km/h only marginally differs from the acceleration at 500 km/h when it hits the girder. This occurs because the 10th vehicle at 450 km/h is greatly excited by the girder in resonance when the 10th train passes through the girder.

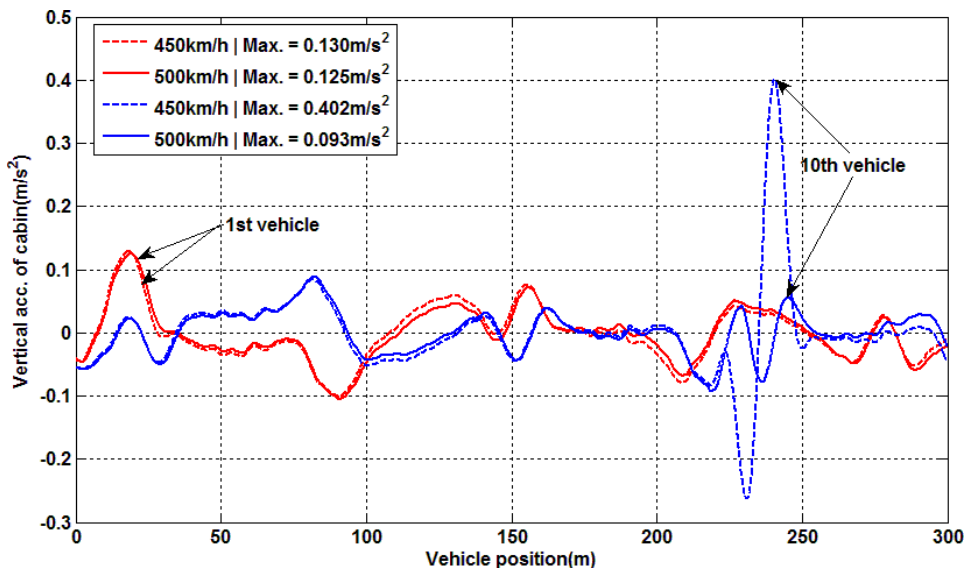


Fig. 19. Vertical acceleration of the first and the last vehicle with 450 and 500 km/h for $d_v = 24.2$ m.

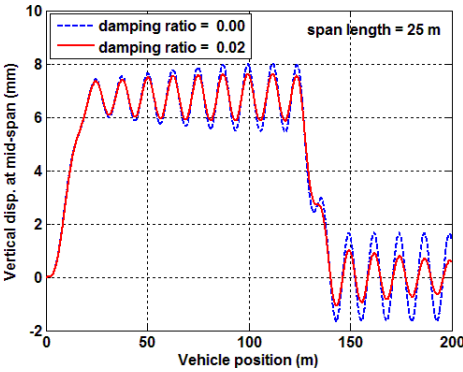
5.3.2. Cancellation condition of a girder under a series of vehicles

To demonstrate the validity of the cancellation condition of Eq. (45) in maglev systems, four girder models are taken into account as shown in Table 6, in which their span length and elastic modulus differ, but the natural frequencies of the four girders are identical. Consequently, a sequence of vehicles moving at the speed of 223.5 km/h should cause a resonant vibration to the four girders under d_v of 12.1 m. However, the second and the fourth girders are not expected to show any resonant behaviors because L_b/d_v of the second and fourth girder satisfy the cancellation condition of Eq. (45).

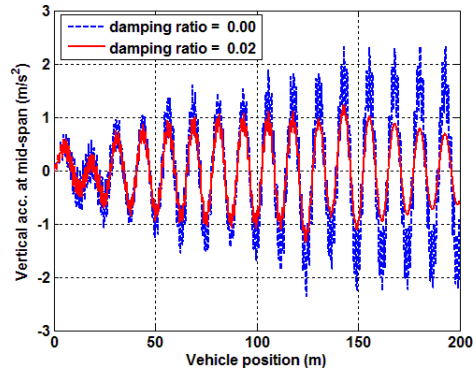
Figure 20 shows the vertical displacements and accelerations at the center of the girder, with four span lengths changed and damping ratios of 0.02 and 0.0. As expected, some resonant behaviors are observed in Figs. 20(a) and 20(b) and Figs. 20(e) and 20(f), but large fluctuations are not shown in Figs. 20(c) and 20(d) and Figs. 20(g) and 20(h) corresponding to the second and fourth span lengths, respectively.

Table 6. Properties of guideway model for various span lengths.

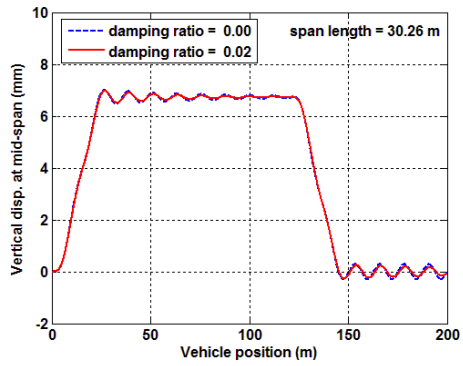
Index	Values			
Span length L_b	25 m	30.26 m	35 m	42.36 m
L_b/d_v	2.07	2.5	2.89	3.5
Elastic modulus E (N/m ²)	3.00×10^{10}	6.44×10^{10}	1.15×10^{11}	2.47×10^{11}
The first natural frequency	5.13 Hz			



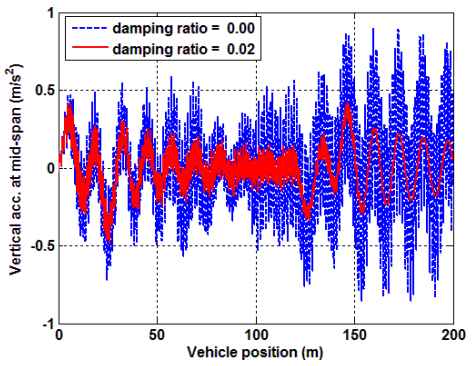
(a) Vertical disp. at mid-span for $L_b = 25$ m.



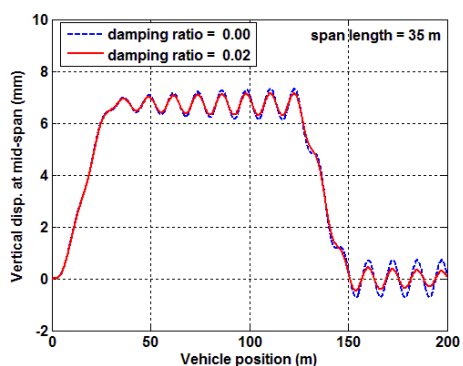
(b) Vertical acc. at mid-span for $L_b = 25$ m.



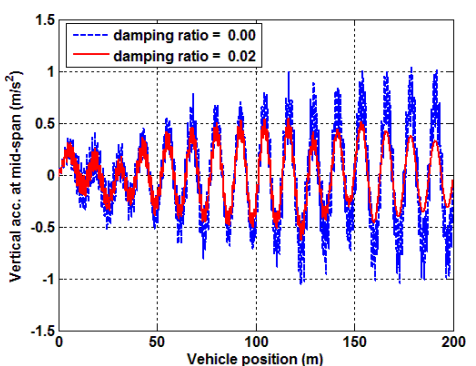
(c) Vertical disp. at mid-span for $L_b = 30.26$ m.



(d) Vertical acc. at mid-span for $L_b = 30.26$ m.

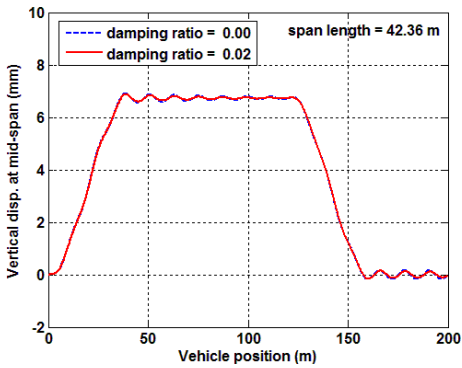


(e) Vertical disp. at mid-span for $L_b = 35$ m.

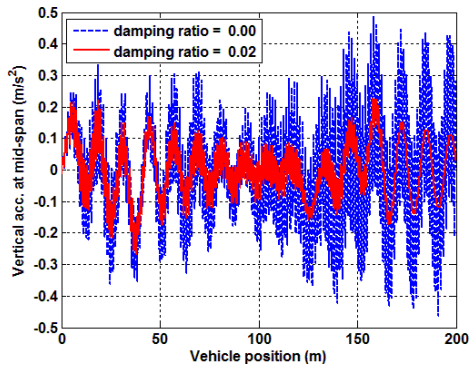


(f) Vertical acc. at mid-span for $L_b = 35$ m.

Fig. 20. Cancellation of resonance on the girder for various span lengths.

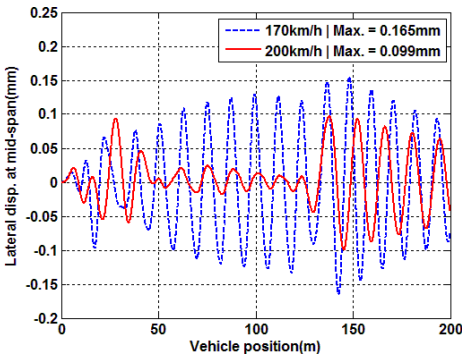


(g) Vertical disp. at mid-span for $L_b = 42.36$ m.

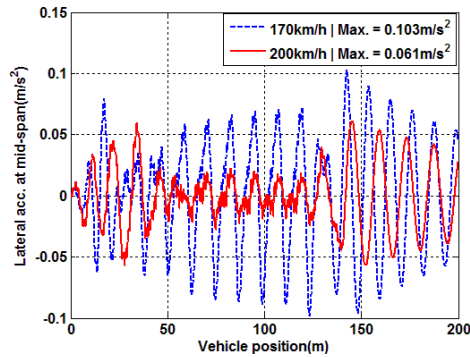


(h) Vertical acc. at mid-span for $L_b = 42.36$ m.

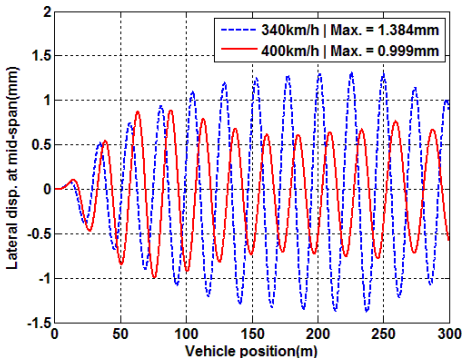
Fig. 20. (Continued)



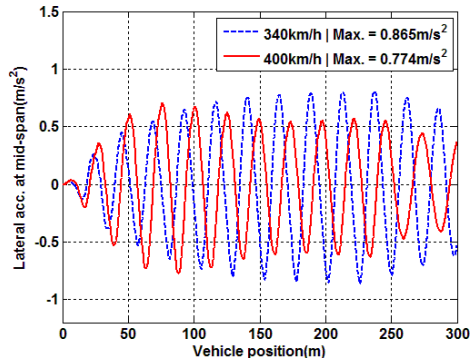
(a) Lateral disp. at mid-span for $d_v = 12.1$ m.



(b) Lateral acc. at mid-span for $d_v = 12.1$ m.



(c) Lateral disp. at mid-span for $d_v = 24.2$ m.



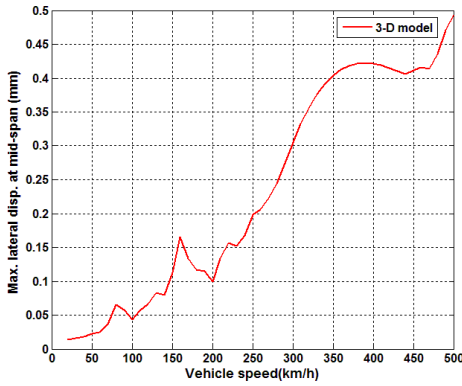
(d) Lateral acc. at mid-span for $d_v = 24.2$ m.

Fig. 21. Time history responses of the girder at vehicle speeds of 170 and 200 km/h.

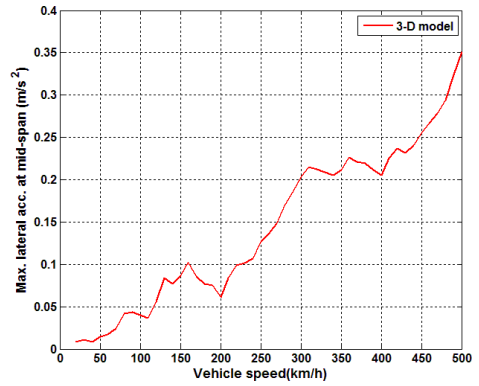
5.4. Lateral resonance of a guideway girder under a series of vehicles

The inertia forces of vehicles caused by lateral surface irregularities produce resonant vibrations on the girder in the lateral direction. In this regard, the lateral resonance speeds can be determined by inserting the first lateral natural frequency f_{ym} (3.94 Hz) into Eq. (46). Consequently, the fundamental resonance speeds of 171.6 km/h ($= 3.6 \times 3.94 \times 12.1$) and 343.3 km/h ($= 3.6 \times 3.94 \times 24.2$) corresponding to $d_v = 12.1$ and 24.2 m, respectively, are calculated.

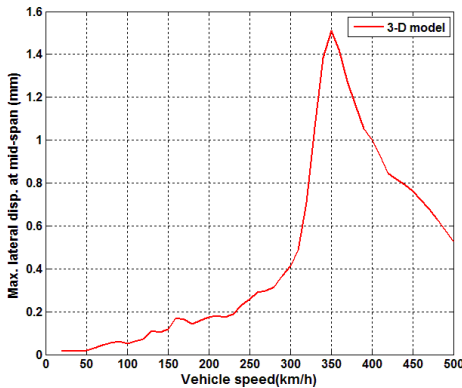
Basically, the 3D dynamic interaction analyses performed in Sec. 5.3.1 provide the lateral responses of the vehicles and girders as well as the vertical responses. Figures 21(a) and 21(b) show the lateral displacement and acceleration at the center of the girder when a series of 10 maglev vehicles have been passed on the guideway at the speeds of 170 and 200 km/h, for $d_v = 12.1$ m. Also, Figs. 21(c) and 21(d) show the lateral displacement and acceleration for the speeds of 340 and 400 km/h, with



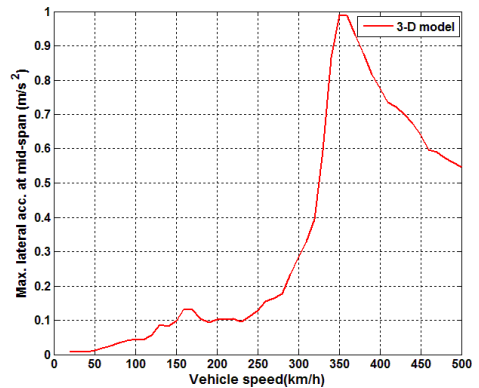
(a) Lateral disp. at mid-span for $d_v = 12.1$ m.



(b) Lateral acc. at mid-span for $d_v = 12.1$ m.



(c) Lateral disp. at mid-span for $d_v = 24.2$ m.



(d) Lateral acc. at mid-span for $d_v = 24.2$ m.

Fig. 22. Maximum lateral responses by increasing vehicle speed with a series of 10 vehicles.

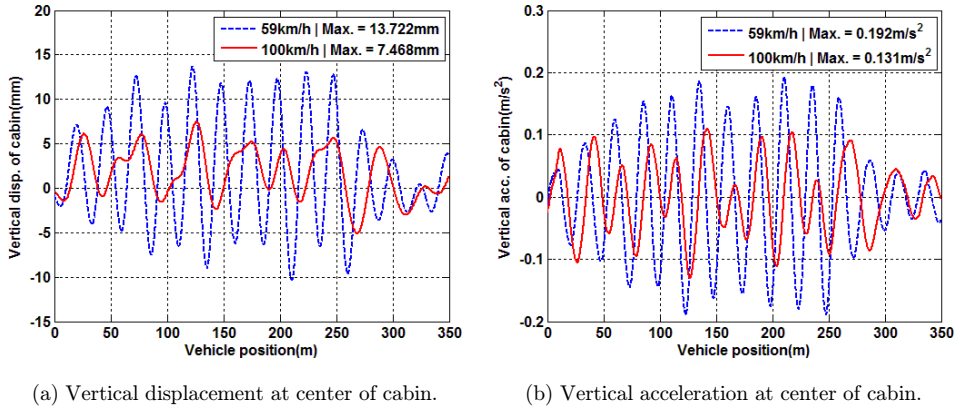


Fig. 23. Time history responses of cabin at vehicle speeds of 59 and 100 km/h.

$d_v = 24.2$ m. Similarly to the vertical resonance of the guideway girders under a series of vehicles, it is observed from Fig. 21 that the girder response continues to increase linearly whenever one vehicle passes on the guideway with the resonance speeds of around 170 and 340 km/h, even though the amplitude is very small because it is caused by the average lateral roughness profiles.

In addition, the maximum girder response in the lateral direction is plotted against the vehicle speed in Fig. 22. Clearly, resonant vibrations are observed at the resonance speed of around 170 km/h and its half speed of 85 km/h for $d_v = 12.1$ m and 340 and 170 km/h for $d_v = 24.2$ m, respectively. Particularly, a dominant peak caused by resonant vibrations is detected at the lateral resonance speed of 350 km/h for $d_v = 24.2$ m.

5.5. Resonances of a maglev vehicle running on multi-girders

Lastly, the resonant vibrations of one vehicle traveling on a sequence of 10 simply supported girders are investigated based on Eq. (49) because the repetition of bridge deflections can cause a maglev vehicle to have resonant behaviors. From the free vibration analysis of one maglev vehicle, the vertical frequency of the cabin f_v is calculated to be 0.65 Hz $\left(= \frac{1}{2\pi} \sqrt{\frac{16k_z}{m_c}} = \frac{1}{2\pi} \sqrt{\frac{16 \times 2 \times 10^4}{19000}} \right)$. The vertical resonance speed of the vehicle from Eq. (49) can be calculated as 58.8 km/h.

Figure 23 shows the vertical displacement and acceleration of the cabin when one maglev vehicle runs on 10 simply supported girders with speeds of 59 and 100 km/h, respectively. For the resonance speed of 59 km/h, it is noted that the vertical response of the cabin continues to increase linearly until the vehicle passes through the last girder. Also, the spectrum of the vertical acceleration for 59 km/h shown in Fig. 24, shows a peak near 0.65 Hz. Also, from the maximum response of the cabin shown in Fig. 25, we observe a sharp peak of maximum vertical displacements and accelerations at the center of the cabin at around 60 km/h. Moreover, Fig. 26 shows

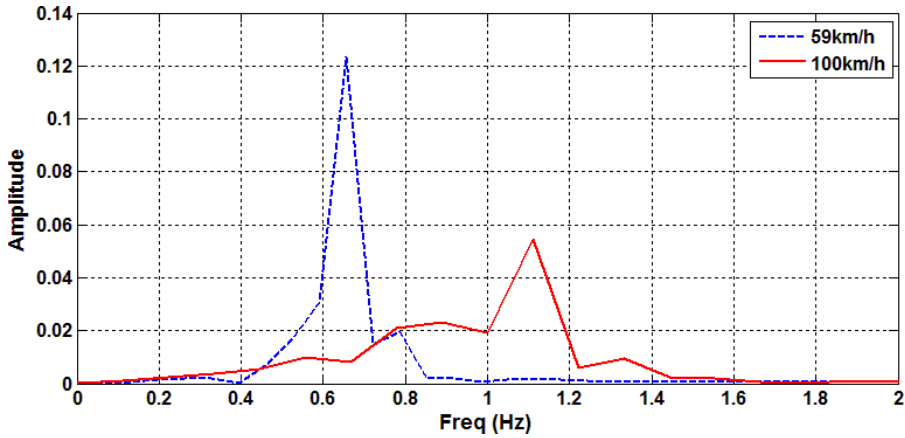


Fig. 24. Spectra of vertical acceleration at center of cabin at vehicle speeds of 59 and 100 km/h.

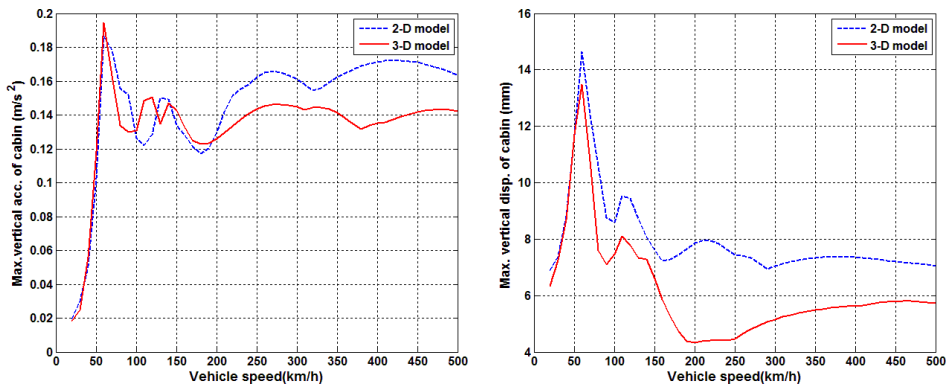
the cabin responses at the resonance speed when the damping coefficient of the secondary suspension in the vertical direction is taken as C_z , $C_z/2$, $C_z/5$, respectively. The resonance phenomena are observed more clearly in Fig. 26.

In addition, the pitching resonance of the cabin can be explored based on the work of Yang and Yau.³⁷ The pitching frequency f_p of the cabin is calculated as 0.77 Hz

$$\left(= \frac{1}{2\pi} \left(\sum_{j=1}^{N_{bogi}/2} \sum_{i=1}^{N_{spring}/2} \sqrt{\frac{k_z}{2I_{cy}} (2a_{jx} + 2b_{ix})^2} \right) \right),$$

which leads to the pitching resonance speed of 69.9 km/h.

Figure 27(a) shows the fluctuation of the maximum pitching acceleration with a sharp peak at around 70 km/h as the vehicle speed is increased, and Fig. 27(b) shows the pitching acceleration of the cabin for the two cases of C_z and $C_z/5$ at the expected



(a) Max. vertical displacement at center of cabin. (b) Max. vertical acceleration at center of cabin.

Fig. 25. Maximum response versus vehicle speed for a series of 10 girders.

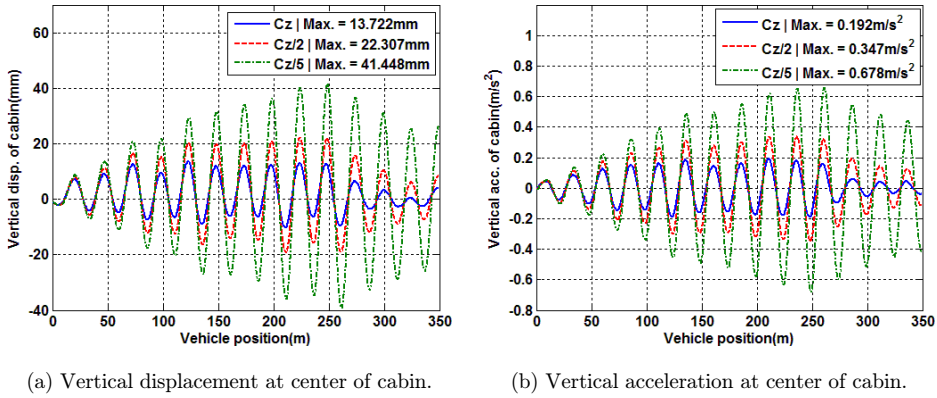


Fig. 26. Resonant vibrations of the cabin for various damping coefficients at 59 km/h.

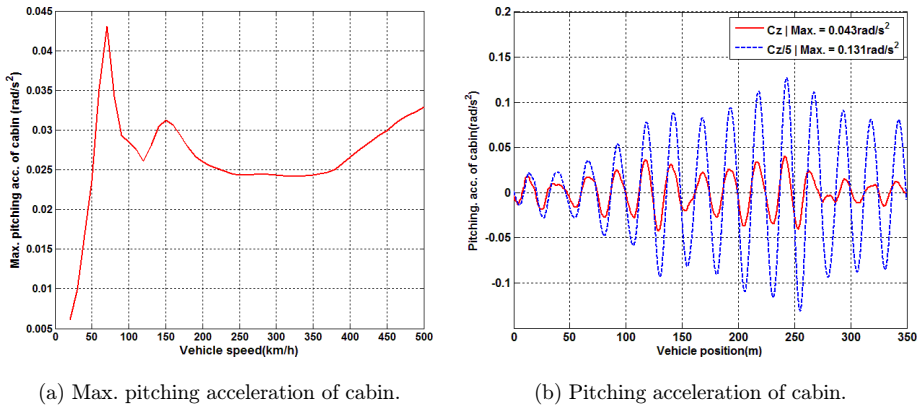


Fig. 27. Resonant vibrations of pitching acceleration responses.

pitching resonance speed of 70 km/h. The resonant pitching vibrations are clearly observed at the resonance speed.

6. Conclusions

In this study, a detailed 3D vehicle model is presented for actively controlled maglev vehicle-guideway systems to realistically investigate the dynamic interaction effects of guideways and vehicles, including vertically and laterally resonant vibrations. The dynamic governing equations of the vehicle-girder system are rigorously derived, and its coupled equations are solved using the predictor–corrector iteration scheme. From numerical analyses, the following conclusions can be drawn:

- (1) A 3D maglev vehicle model consisting of one cabin and four bogies is proposed by adopting the actively controlled eight EMS per bogie and considering the lateral as well as vertical roughness profiles.

- (2) The dynamic interaction analysis procedures of the 3D maglev system and the corresponding 2D system are developed by superposing the mode shapes of the girder. It is found from the analysis results that, while the time history responses obtained for the two systems are very similar, the dynamic responses of the cabins show a slight difference because the vehicles are relatively sensitive to the roughness in the vertical and lateral directions.
- (3) The vertical resonant behaviors of the single girder under a series of 10 vehicles are clearly detected at the fundamental resonance speeds of the vehicles, which are analytically predicted from the dynamic responses of a simple girder under equidistant moving loads. Meanwhile, any increasing fluctuations are not observed at the resonance speed whenever the cancellation condition is satisfied.
- (4) The 3D dynamic interaction analyses show that the laterally resonant vibrations of the girder clearly occur at around the predicted resonance speeds because of the inertia forces of vehicles caused by the lateral surface irregularities, but their amplitudes are found to be very small.
- (5) Lastly, the vertical and pitching resonant behaviors of the cabin are induced at the expected resonance speed for one vehicle traveling on a sequence of 10 simply supported girders. The above observations are consistent with those of Refs. 33 and 37.

References

1. Y. Cai, S. and S. Chen, A review of dynamic characteristics of magnetically-levitated vehicle systems, *Applied Mechanics Reviews*, *Trans. ASME* **50**(11) (1997) 647–670.
2. H. Alschér, M. Iguchi, A. R. Eastham and I. Boldea, Non-contact suspension and propulsion technology, *Veh. Syst. Dyn.* **12** (1983) 259–289.
3. K. Popp and W. Schiehlen, Dynamics of magnetically levitated vehicles on flexible guideways, *Proc. IUTAM Symp. on the Dynamics of Vehicles on Roads and Railway Tracks*, Delft (1975), pp. 479–503.
4. K. Popp, Contributions on dynamics of maglev vehicles on elevated guideway, *Fortschr.-Berichte VDI-Zeitschrift*. **12**(35) (1978).
5. G. Bohn and G. Steinmetz, The electromagnetic suspension system of the magnetic train ‘transrapid’, *Proc. Int. Conf. Maglev Transrapid85* (1985) 57–71.
6. S. Yamamura, Magnetic levitation technology of tracked vehicle present status and prospects, *IEEE Trans. Magn.* **12** (1976) 874–878.
7. M. Miyamoto, A dynamic response of magnetically levitated flexible vehicle to random track irregularities, *Q. Rep. RTRI* **21**(1) (1980) 44–48.
8. X. J. Zheng, J. J. Wu and Y. H. Zhou, Numerical analysis on dynamic control of five-degree-of-freedom maglev vehicle moving on flexible guideways, *J. Sound Vib.* **235**(1) (2000) 43–61.
9. D. F. Zhao and W. M. Zhai, Maglev vehicle/guideway vertical random response and ride quality, *Vehi. Syst. Dyn.* **38**(3) (2002) 185–210.
10. H. P. Wang, J. Li and K. Zhang, Vibration analysis of the maglev guideway with the moving load, *J. Sound Vib.* **305**(4–5) (2007) 621–640.
11. J. Yang, A. Zoltas, W. H. Chen, K. Michail and S. Li, Robust control of nonlinear MAGLEV suspension system with mismatched uncertainties via DOBC approach, *ISA Trans.* **50**(3) (2011) 389–396.

12. J. Shi and Y. J. Wang, Dynamic response analysis of single-span guideway caused by high speed maglev train, *Lat. Am. J. Solids Struct.* **8** (2011) 213–228, pp. 935–941.
13. Y. Cai, S. S. Chen, S. M. Rote and H. T. Coffey, Vehicle/guideway interaction for high speed vehicles on a flexible guide-way, *J. Sound Vib.* **175**(5) (1994) 625–646.
14. J. Fang, A. Radovinsky and D. B. Montgomery, Dynamic modeling and control of the Magplane vehicle, in *Maglev2004* (Shanghai, 2004), pp. 935–941.
15. J. Kaloust, C. Ham, J. Siehling, E. Jongekryg and Q. Han, Nonlinear robust control design for levitation and propulsion of a maglev system, *IEE Proc., Control Theory Appl.* **151**(4) (2004) 460–464.
16. C. M. Huang, M. S. Chen and J. Y. Yen, Adaptive nonlinear control of repulsive Maglev suspension systems, *IEEE Int. Conf. Control Applications 1999* (Hawaii, USA, 1999), pp. 1734–1739.
17. J. D. Yau, Vibration control of maglev vehicles traveling over a flexible guideway, *J. Sound Vib.* **321**(1–2) (2009) 184–200.
18. J. D. Yau, Interaction response of maglev masses moving on a suspended beam shaken by horizontal ground motion, *J. Sound Vib.* **329**(2) (2010a) 171–188.
19. J. D. Yau, Aerodynamic vibrations of a maglev vehicle running on flexible guideways under oncoming wind actions, *J. Sound Vib.* **329**(1) (2010b) 1743–1759.
20. J. D. Yau, Lateral vibration control of a low-speed maglev vehicle in cross winds, *Wind Struct.* **15**(3) (2012) 263–283.
21. H. Yaghoubi and M. A. Rezvani, Development of maglev guideway loading model, *J. Trans. Eng.* **137**(3) (2011) 201–213.
22. R. Shibo, R. Arie and K. Kees, Dynamic simulation of the maglev vehicle/guideway system, *J. Bridge Eng.* **15**(3) (2010) 269–278.
23. S. H. Han, Y. J. Kim, B. C. Shin and B. H. Kim, Simulation of dynamic interaction between maglev and guideway using FEM, *Maglev2006* (Dresden, Germany, 2006).
24. B. M. Jin, I. G. Kim, Y. J. Kim and I. H. Yeo, W. S. Chung and J. S. Moon, Proposal of maglev guideway girder by structural optimization: Civil works of Center for Urban Maglev Program in Korea, in *Proc. Int. Conf. Electrical Machines and Systems* (Seoul, Korea, 2007), pp. 1959–1962.
25. S. D. Kwon, J. S. Lee, J. W. Moon and M. Y. Kim, Dynamic interaction analysis of urban maglev vehicle and guideway suspension bridge subjected to gusty wind, *Eng. Struct.* **30**(12) (2008) 3445–3456.
26. J. S. Lee, S. D. Kwon, M. Y. Kim and I. H. Yeo, A parametric study on the dynamics of urban transit maglev vehicle running on flexible guideway bridges, *J. Sound Vib.* **328**(3) (2009) 301–317.
27. D. J. Min, J. S. Lee and M. Y. Kim, Dynamic interaction analysis of actively controlled maglev vehicles and guideway girders considering nonlinear electromagnetic forces, *Coupled Syst. Mech.* **1**(1) (2012) 39–57.
28. P. K. Sinha, *Electromagnetic Suspension-Dynamics and Control* (IEE, London, United Kingdom, 1987).
29. V. K. Garg and R. V. Dukkipati, *Dynamics of Railway Vehicle Systems* (Academic Press, New York, 1984).
30. D. A. Hullender, Analytical models for certain guideway irregularities, *J. Dyn. Syst., Meas. Control* **97**(4) (1975) 417–423.
31. Q. Zou, L. Deng, T. Guo and X. Yin, Comparative study of different numerical models for vehicle-bridge interaction analysis, *Int. J. Struct. Stab. Dyn.* **16** (2016) 1550057.
32. L. Fryba, *Dynamics of Railway Bridges* (T. Telford, Prague, Czech Republic, 1996).
33. Y. B. Yang, J. D. Yau and L. C. Hsu, Vibration of simple beams due to trains moving at high speeds, *Eng. Struct.* **19**(11) (1997) 936–944.

34. H. Xia, N. Zhang and W. W. Guo, Analysis of resonance mechanism and conditions of train-bridge system, *J. Sound Vib.* **297** (2006) 810–822.
35. Y. L. Xu, Q. Li, D. J. Wu and Z. W. Chen, Stress and acceleration analysis of coupled vehicle and long-span bridge systems using the mode superposition method, *Eng. Struct.* **32** (2010) 1356–1368.
36. Y. J. Wang, Q. C. Wei and J. D. Yau, Interaction response of train loads moving over a two-span continuous beam, *Int. J. Struct. Stab. Dyn.* **13** (2013) 1350002.
37. Y. B. Yang and J. D. Yau, Vertical and pitching resonance of train cars moving over a series of simple beams, *J. Sound Vib.* **337** (2015) 135–149.